Contents lists available at GrowingScience

Engineering Solid Mechanics

homepage: www.GrowingScience.com/esm

On the effect of heat treatment schedules on the structure-property behaviour of heat-affected zones of ASTM A335 steel: Gleeble thermal-mechanical simulation

Japheth Obiko[a,b*], David Whitefield[a] and Micheal Bodunrin[a]

[a]*University of the Witwatersrand, School of Chemical and Metallurgical Engineering, 1 Jan Smuts Avenue, Johannesburg, 2000, South Africa*
[b]*Jomo Kenyatta Univesity of Agriculture and Technology, Department of Mining, Materials and Petroleum Engineering, Nairobi, Kenya*

ARTICLE INFO

Article history:
Received 10 July 2024
Accepted 15 January 2025
Available online
15 January 2025

Keywords:
Normalisation
Tempering
P92 steel
Weld joint
Gleeble simulation
Type IV cracking

ABSTRACT

This study reports on microstructure evolution and mechanical properties of weld joints of two ASTM A335 P92 steels with varying chromium and tungsten content influenced by heat treatment. Physical simulation samples for fine-grain and intercritical heat-affected zones were done using the Gleeble® 3500 equipment. A peak temperature of 900°C (intercritical zone) and 950°C (fine-grained zone) simulated different heat-affected zones. After physical simulation, the test samples underwent two heat treatment schedules: post-weld heat treatment (PWHT) and normalisation, followed by tempering. The results show that the two steels had similar martensite microstructure. The microstructure further exhibited the presence of M23C6 carbides along the grain and lath boundaries. The P92-B steel had the highest hardness values after heat treatment except at FGHAZ + PWHT condition, which had a lower hardness value (271.9 ± 5.0 HV0.5). In this condition (FGHAZ + PWHT), P92-B steel had a higher Charpy toughness value (180J), slightly higher than the base metal (178J) due to fully formed martensite microstructure. ICHAZ + heat treatment, P92-B steel had the lowest toughness values (74J for r-PWHT and 83J for PWHT), but these values were higher than the minimum toughness value of 47J of the weld joint required for hydro-testing of the vessels. The study revealed no marked significant differences between the two steels. The heat treatment method (r-PWHT) is applicable in the industry for Type IV crack mitigation of the weld joint.

1. Introduction

Demand for electrical energy for industrial development and domestic use has increased tremendously (Guo et al., 2015). Fossil fuel is used extensively for power generation. Most fossil-fuel power plants now operate under ultra-supercritical (USC) technology. These power plants operate at a steam temperature of ~650°C and a steam pressure of 35 MPa (Francis et al., 2006). The heat efficiency of fossil-fuel power plants has been increased by 45% to reduce CO_2 emissions (Ennis & Czyrska-Filemonowicz, 2003). The 9-12% Cr steels were developed for these power plant components since they can withstand severe working conditions in nuclear and fossil-fuel power plants (Francis, Mazur & Bhadeshia, 2006, Sakthivel *et al.*, 2014). These steels have applications in boiler tubing systems, rotors, and turbine castings due to their high creep resistance, fabricability, and corrosion resistance during service (Nagode et al., 2011). In the early 1970s, Oak Ridge Laboratory in the USA developed P91 steel for power plant components with additions of molybdenum, niobium, and vanadium for improved creep resistance (Hurtado-noreña et al., 2015). Solid solution strengthening occurs due to the formation of carbides along the laths and grain boundaries and carbonitrides in the matrix, thus increasing creep strength (Łomozik & Zielińska-Lipiec, 2008). However, the creep strength and oxidation resistance of P91 steel decrease at temperatures above 600°C (Milović et al., 2013). Nippon Steel in Japan developed NF616 steel by modifying P91 steel by adding 1.8% W and reducing Mo by 0.5% (Francis et al., 2006). This steel is designated in the ASTM specifications as P92 steel (Ennis & Czyrska-Filemonowicz, 2003). The P92 steel has a ~30% higher creep strength than P91 steel under the same service conditions (Ohgami et al., 1997; Sklenička et al., 2016). Tungsten and molybdenum additions enhance creep strength due to solid solution strengthening (Czyrska-filemonowicz et al., 2006).

* Corresponding author.
E-mail addresses: japheth.obiko97@gmail.com (J. Obiko)

ISSN 2291-8752 (Online) - ISSN 2291-8744 (Print)

doi: 10.5267/j.esm.2025.1.002

The joining of power plant components is by welding. During welding, the material experiences different weld thermal cycles, causing the formation of a soft zone (Pandey *et al.* 2019). This zone has poor creep strength and may cause premature failure of welded structures after long-term service (Lim et al., 2003). These zones formed during welding due to different weld thermal cycles, as shown in **Fig. 1** (Francis et al., 2006). Creep failure occurs due to microcracks initiation, especially in the heat-affected zone (HAZ) of the weld joint (Abson & Rothwell, 2013; Tabuchi et al., 2001). Weld joint cracks are classified according to the position of crack initiation and propagation (Abson & Rothwell, 2013). Type I and Type II cracks usually occur in the weld metal and grow within the weld metal. However, Type II cracks may also propagate through the weld metal into the HAZ and the parent metal. Type III cracks nucleate in the coarse-grained heat-affected zone. The fine-grained heat-affected region provides the mechanism for the initiation of Type-IV cracks. These cracks cause premature failure in the weld joints (Francis et al., 2006). The Type IV crack initiation and propagation are accelerated by high-stress triaxiality (state of stress) in this region, causing localized strain accumulation under creep conditions (Esposito, 2016). The initiation and propagation of Type IV crack occurs at the HAZ surface near the base metal. However, the position of Type IV crack initiation remains unclear. Most researchers report that Type IV cracks occur at the intercritical (ICHAZ) or the FGHAZ regions (Abson & Rothwell, 2013).

Studies show that Type IV cracking contributes to failure mechanisms in welded structural power plant components (Tabuchi et al., 2001), (Vodopivec et al., 2011). The failures occur in the heat-affected zone (HAZ), which undergoes microstructural changes due to the weld thermal cycle (Albert et al., 2003; X. Wang et al., 2014; Xue et al., 2012). The microstructural regions in the HAZ are (Gutiérrez et al., 2015) as follows:

1. *Coarse-grained HAZ (CGHAZ)*: is located near the fusion line and experiences high peak temperature above the $(\alpha+\gamma) / \gamma$ (Ae3) boundary. During the thermal cycle, phase transformation to austenite occurs. Dissolution of carbides is experienced in this region. This phenomenon causes coarse austenite grains formation. The CGHAZ region is about 200 µm wide.

2. *Fine-grained HAZ (FGHAZ)*: undergoes complete austenite transformation at peak temperatures above Ae3. The region exhibits finer austenite grains, which later transform to martensite on cooling for 9-12 wt.%Cr heat-resistant steels. The FGHAZ is susceptible to Type IV cracking.

3. *Intercritical HAZ (ICHAZ)*: occurs ~2.5 mm from the fusion line but adjacent to the parent metal. This region experiences a peak temperature between the lower (Ae1) and upper (Ae3) critical phase transformation temperature during the welding, resulting in the partial transformation of martensite to austenite.

Type IV cracks nucleate and propagate through the heat-affected zone (HAZ) in weld joints (Tabuchi et al., 2001; Tanaka et al., 2013; Xue et al., 2011; Zhao et al., 2014). In high Cr steel containing tungsten, Tabuchi *et al.* (2001) reported that creep failure occurred due to Type IV cracks in the HAZ for electron beam welded (EBW) joints. Shankar *et al.*(2013) showed that low-cycle fatigue damage in P91 steel occurred in the HAZ. They observed micro-voids in the HAZ, resulting in the nucleation of a fatal crack, which caused the failure. The study further noted that at 600°C, the initiated crack propagated within the HAZ, a characteristic feature of Type IV cracking. However, at a lower temperature of 500°C, crack initiation occurred at the HAZ region but later propagated towards the weld metal (Shankar et al., 2013). Sakthivel *et al.*(2014) reported that more microvoids formed in the simulated FGHAZ of P92 steel than in other regions of the weld joint. Another study reported that microvoids formed in the ICHAZ due to creep damage, which coalesced to form Type IV cracks (Hasegawa et al., 2009). Peng *et al.* (2017) and Barbadikar *et al.* (2018) showed that the simulated ICHAZ in P92 steel had the lowest strength and hardness, and failure occurred due to Type IV cracking. It is clear from the literature that two issues need attention: (1) the location of Type IV cracks and (2) their prevention mechanisms. To this end, the influence of microstructure evolution in the weld joint (especially HAZ) on mechanical properties, especially for P92 steel, is scanty in the literature.

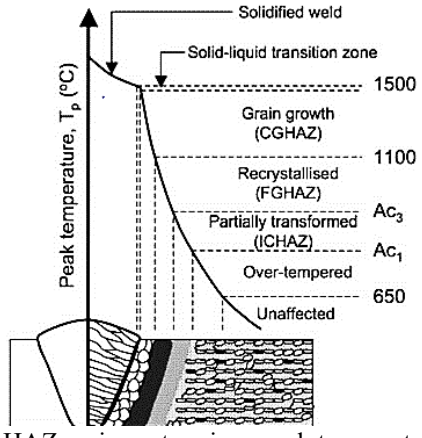

Fig. 1. An illustration of HAZ regions at various peak temperatures (Francis et al., 2006).

The literature has shown that the weld joint has a heterogeneous microstructure, which negatively affects the mechanical properties such as toughness, thus causing creep failure during industrial application. Therefore, achieving uniform microstructure across the weld joint is of great concern. This current study explored the effect of heat treatment (PWHT and N + T) on the microstructure evolution of physically simulated HAZ microstructure of two P92 steel having variations in chemical composition. The study will further provide information on the effect of the homogenisation process (N+T) on the heat-affected zones of P92 steel on mechanical properties.

2. Experimental procedure

The P92 steel is normally supplied in normalization and tempering (N + T) conditions. The elemental composition of the two steels studied is shown in **Table 1.** These two steels are herein denoted as P92-A and P92-B. The as-received plates were sectioned to the dimension of 70 mm × 10 mm × 10 mm which is the standard HAZ physical simulation sample used in the Gleeble®3500 equipment. A single-pass physical HAZ simulation was done for each specimen. The simulation temperature was controlled using K-type thermocouples spot-welded mid-height of the test specimen. The simulation thermal history is shown in **Fig. 1**, which involves:

1. Heating to the weld HAZ peak temperature (T_{max}) at temperature of 60 °C per second.
2. The peak temperatures were: ICHAZ (900°C) and FGHAZ (950 °C)
3. Exponential cooling (Figure 1) was used at a specified rate from 800 °C to 500 °C as given by Eq. (1) (Gleeble, 1999):

$$T = T_{max} exp \frac{-0.47t}{\Delta t_{8/5}} \tag{1}$$

where T is the temperature increment per second, T_{max} is the peak temperature, t is the time (sec) and Δt is the cooling time from 800 °C to 500 °C in seconds. The peak temperatures used in this study were within the phase transformation temperature ($Ae_1 \leq T_p \leq Ae_3$) for P92 steel reported in the literature and around Ae3 (Barbadikar et al., 2018; Falat et al., 2016; Peng et al., 2017) and around Ae_3 (Dunđer et al., 2019; Liu et al., 2013, 2014). At the peak temperature, the dwell time was 0.5 s and then cooled at Δt8/5= 20 seconds.

Table 1. Chemical composition (wt.%) of the two steels

Element	C	Mn	Si	Cr	Mo	Ni	Cu	V	Nb	W	Co	Fe
P92-A	0.11	0.51	0.22	9.37	0.5	0.17	0.27	0.19	0.13	1.76	0.028	Bal.
P92-B	0.11	0.32	0.25	9.48	0.61	0.17	0.00	0.20	0.08	2.34	0.024	Bal.

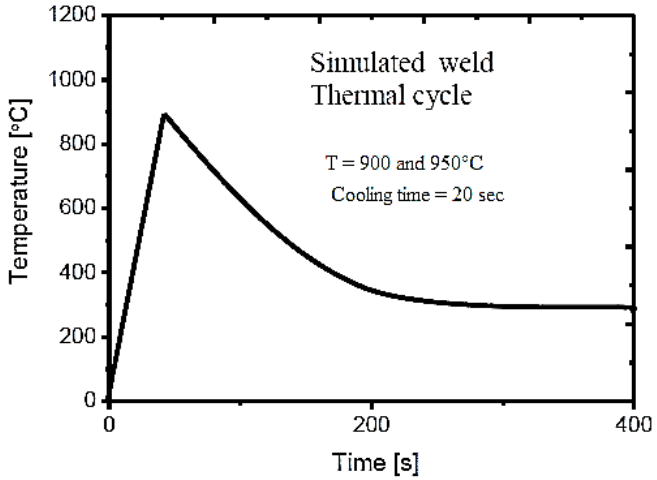

Fig. 2. Thermal cycle of weld joint simulation.

After the physical Gleeble HAZ simulation, the following heat treatment schedule was performed on the HAZ specimens:

1. Conventional post-weld heat treated (PWHT) - tempering the weld joint at 760 °C for 2 hours then air cooling to room temperature (**Fig. 3**).
2. The r-PWHT - austenitising simulated HAZ samples at 1050 °C for 40 minutes, air-cooling to room temperature, tempering at 760 °C for 2 hours, and then air-cooling to room temperature (**Fig. 3**).

The r-PWHT procedure aims to homogenise the simulated HAZ region microstructure. This process rejuvenates the microstructure, hence improving the mechanical properties of steel. Falat *et al.* (2016) reported similar treatment on

T92/TP316H dissimilar weld joints. The HAZ samples were ground and polished following the standard metallographic procedures to study and analyse the microhardness and microstructure. The test samples were etched using Villella's reagent. Leica DM 6000M Zeiss and field emission scanning electron microscopes studied microstructure evolution. The study used a FUTURE-TECH FM-700 microhardness test to measure the microhardness of all test samples using a load (1000g) and a dwell time (10 seconds). Standard Charpy impact testing samples were machined from the HAZ simulated samples, which were as-welded and after heat treatment. Charpy toughness tests were conducted at room temperature per ASTM E23-12c standard (ASTM E 23-12c, 2012). The V-notch was machined at the midspan of the test sample to ensure the notch was in the centre of the HAZ region.

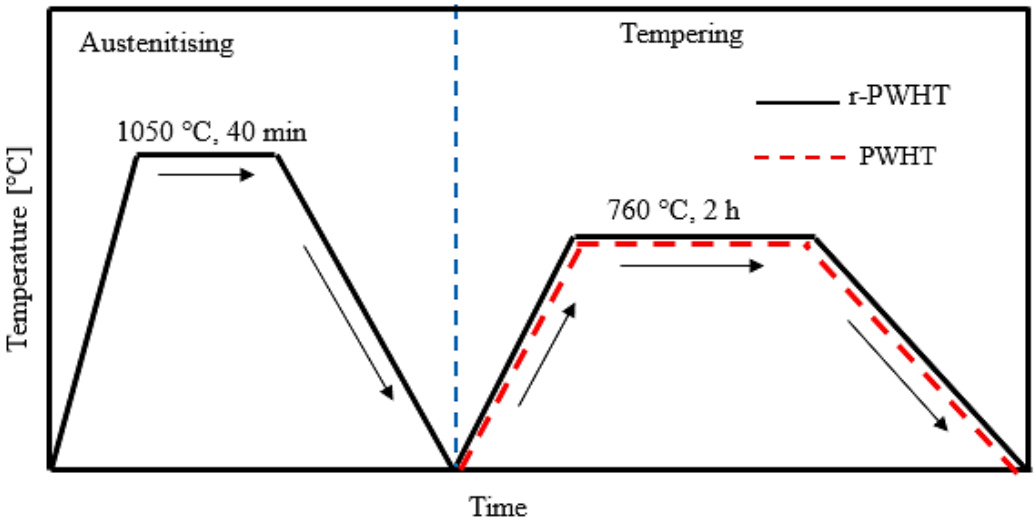

Fig. 3. Schematic diagram of heat treatment for r-PWHT and PWHT.

3. Results and Discussion

3.1. Thermal cycles for physical HAZ simulation

Fig. 4 shows the thermal cycles of the two HAZ simulations of ICHAZ) and FGHAZ. The graphs show an accurate trend between the measured and program temperatures. The phase transformation equilibrium temperatures were determined using analytical solutions developed by Chalk, Shipway, and Allen (Chalk et al., 2011), which is Andrews' model (Trzaska, 2015), as reported by Kim *et al.* (2017). The selected peak temperatures are that: 900 °C lies in the middle of the two-phase region (Ae1 and Ae3), but 950 °C is at or just above the Ae3 for the two P92 steels. The table shows the calculated phase dissolution temperatures for the two P92 steel.

Table 2. Calculated phase transformation temperatures of the two P92 steels.

Model	Trans.	P92-A	P92-B
	T(°C)	°C	°C
Andrews [36]	Ae_3	908	922
Chalk *et al.* [35]	Ae_1	817	850

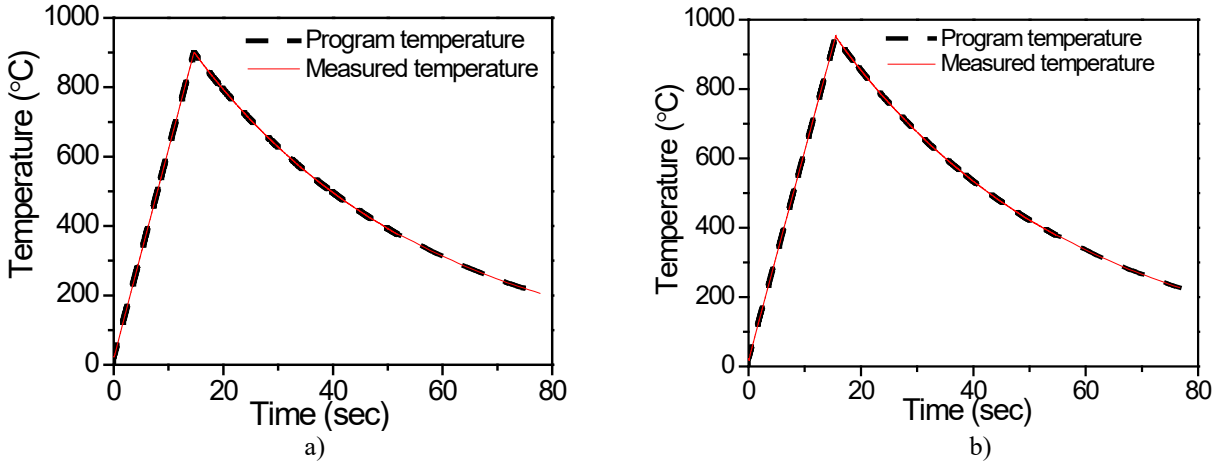

Fig. 4. Thermal cycle for HAZ microstructure simulation using the Gleeble® 3500 thermo-mechanical simulator a) 900 °C, and b) 950 °C.

However, the critical phase transformation temperatures may increase as the heating rate increases during the physical simulation (Peng et al., 2017). The reason is that the dissolution of carbides and martensite laths into austenite is a diffusion-controlled process. These peak temperatures depict the ICHAZ and FGHAZ microstructures after physical simulation. **Fig. 4** shows the thermal cycles for the physical simulation of the ICHAZ (900 °C) and FGHAZ (950 °C). The measured and the program temperature curves were very close throughout the tests (**Fig. 4**). The results show the accuracy of the Gleeble®3500 machine in conducting experimental tests.

3.2. Microstructure of as-received steels

P92 steel undergoes normalisation and tempering conditions before being put into service. **Table 1** shows the elemental composition of the two steels under investigation. In this study, the notation of the two steels was P92-A and P92-B. Figure 5 shows the white precipitates on the grain and lath boundaries of the two P92 steels. The carbides are mostly M23C6 and mainly occur along the grain boundaries (Pandey *et al.,* 2019). The randomly distributed carbonitrides MX precipitates in the matrix (Barbadikar et al., 2015). The coarse carbides at the lath and grain boundaries prevent grain boundary movement and the subgrain dislocations. This structural action resists creep failure (Pandey *et al.*, 2018). The two common precipitates ($M_{23}C_6$ and MX) resist creep failure by hindering grain boundary and dislocation movement (Abson & Rothwell, 2013; Nagode et al., 2011). The visible particles are $M_{23}C_6$ carbides (**Fig. 5**).

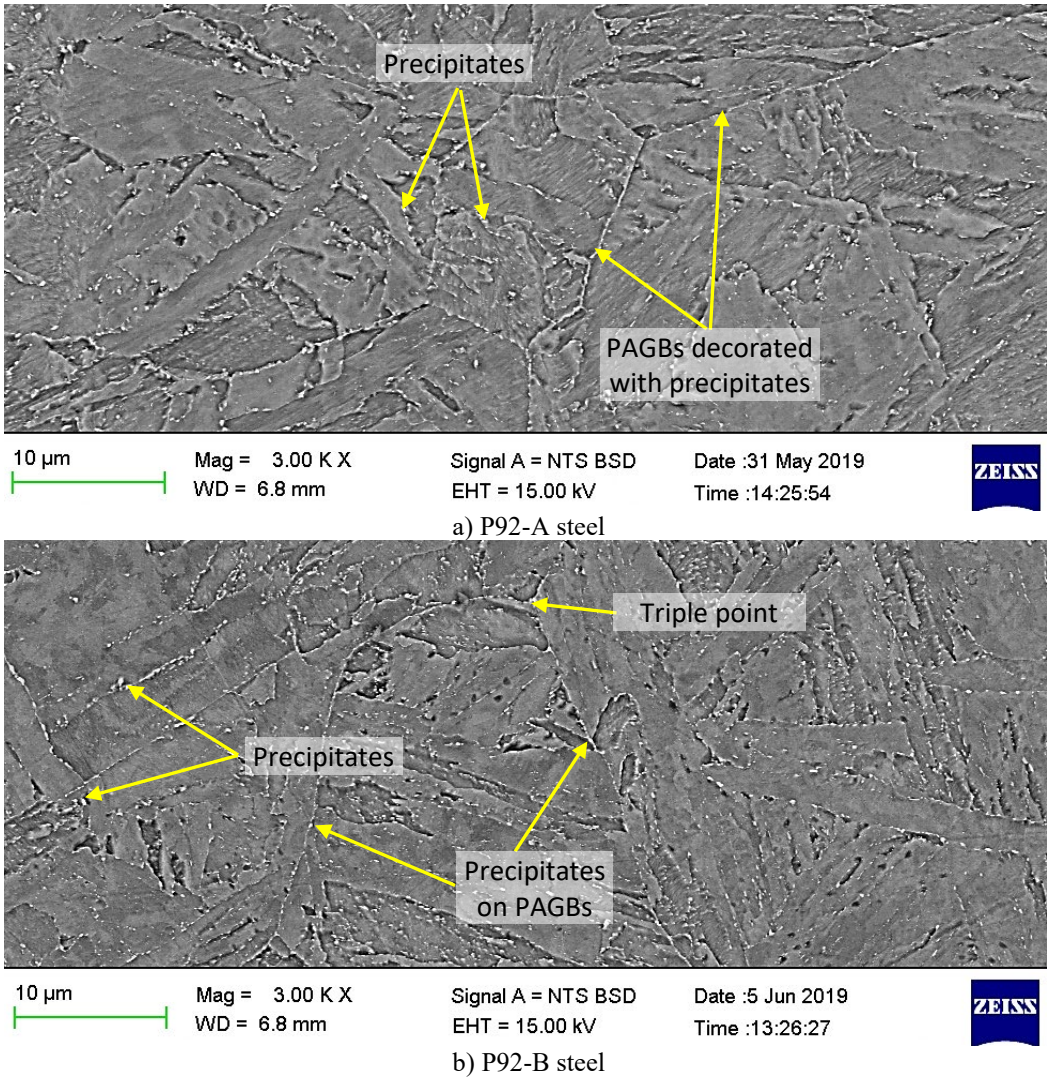

Fig. 5. SEM-BSE micrographs of as-received P92 steels.

Fig. 7 shows the X-ray diffraction (XRD) analysis. The results show the carbides present were $Cr_{23}C_6$, Cr_7C_3, MnC, and V(CN) for P92-A steel and $Cr_{23}C_6$ V_4N_3 Mn_7C_3 for P92-B steel. As mentioned earlier, the carbides occur on the grain boundaries (Pandey *et al.*, 2018). These carbides enhance creep strength by hindering grain boundary motion (Abson & Rothwell, 2013). The MX precipitates provide resistance to deformation (Nagode et al., 2011). Thermo-Calc software predicted the phase transformation and dissolution temperature of precipitates for the two steels. **Fig. 6** shows the results of predicted data of phase volume (%) versus temperature. In the ThermoCalc simulation, the phases identified were $M_{23}C_6$,

MX, and Laves phase. The results show that as the temperature increased, the dissolution of precipitates increased and vice versa (**Fig. 6**).

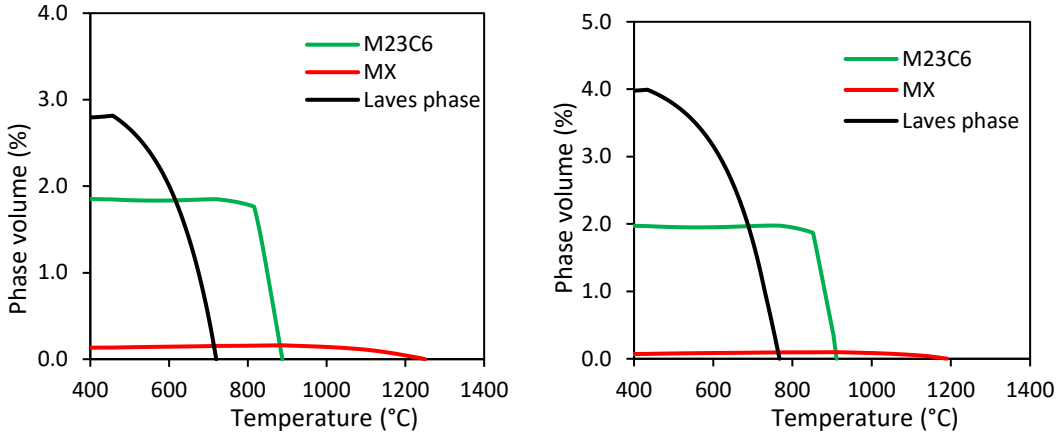

a) P92-A b) P92-B

Fig. 6. Thermo-Calc analysis for the two steels under equilibrium.

Table 3. Precipitate dissolution temperature for the two steels investigated.

Steel	Carbides	MX	Laves
P92-A	888	1250	720
P92-B	911	1192	770

The dissolution temperature of MX precipitates was higher than the other phases (**Fig. 6**). Generally, during normalisation, the carbides ($M_{23}C_6$) dissolve into the solid solution, causing solid-solution hardening. During tempering, precipitation occurs, resulting in phase formation and transformation. Therefore, these results provide a basis for determining the (**Fig. 6**) Ac1 and Ac3 phase transformation temperatures for the physical simulation of HAZ and heat treatment procedures.

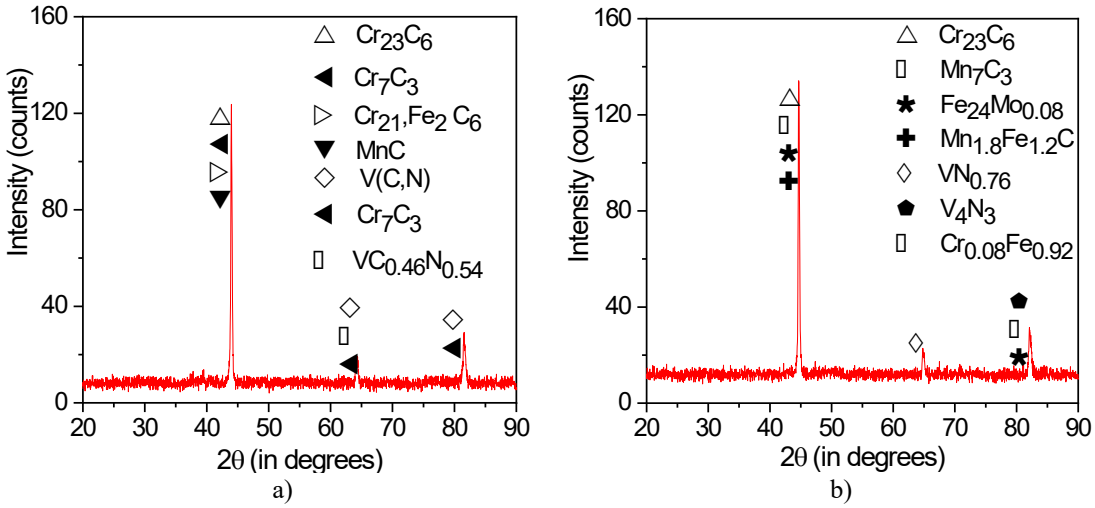

a) b)

Fig. 7. XRD pattern for as-received base metals a) P92-A, b) P92-B.

3.3 Microstructure of as-simulated HAZ

Fig. 8 shows the optical micrographs of as-received and the simulated HAZ microstructures for ICHAZ and FGHAZ for the two steels. The as-received parent metal of the three steels contained tempered martensite with clear prior austenite grain boundaries. The ICHAZ and FGHAZ samples had finer martensite laths than the as-received parent metal. The HAZ peak temperatures were high enough to partially transform some tempered martensite to austenite during heating, which then transformed to untempered martensite on rapid cooling. As-simulated P92-B steel had a few ferrite patches. The observed ferrites form due to incomplete phase transformation during the thermal cycle or alloying element additions (Pandey *et al.*, 2018). During the thermal cycle, carbide dissolution and dislocation annihilation occur, causing carbide-free ferrite formation. Ryu and Yu (1998) reported that ferrite retention is a function of alloying elements which affect austenite field formation. Ferrite minimisation is by optimisation of ferrite stabilisers and the cooling rate. The cooling rate affects the martensite start (M_s) and finishing (Mf)temperature. A higher cooling rate reduces M_s and M_f temperature (Peng et al., 2017), thus preventing ferrite formation.

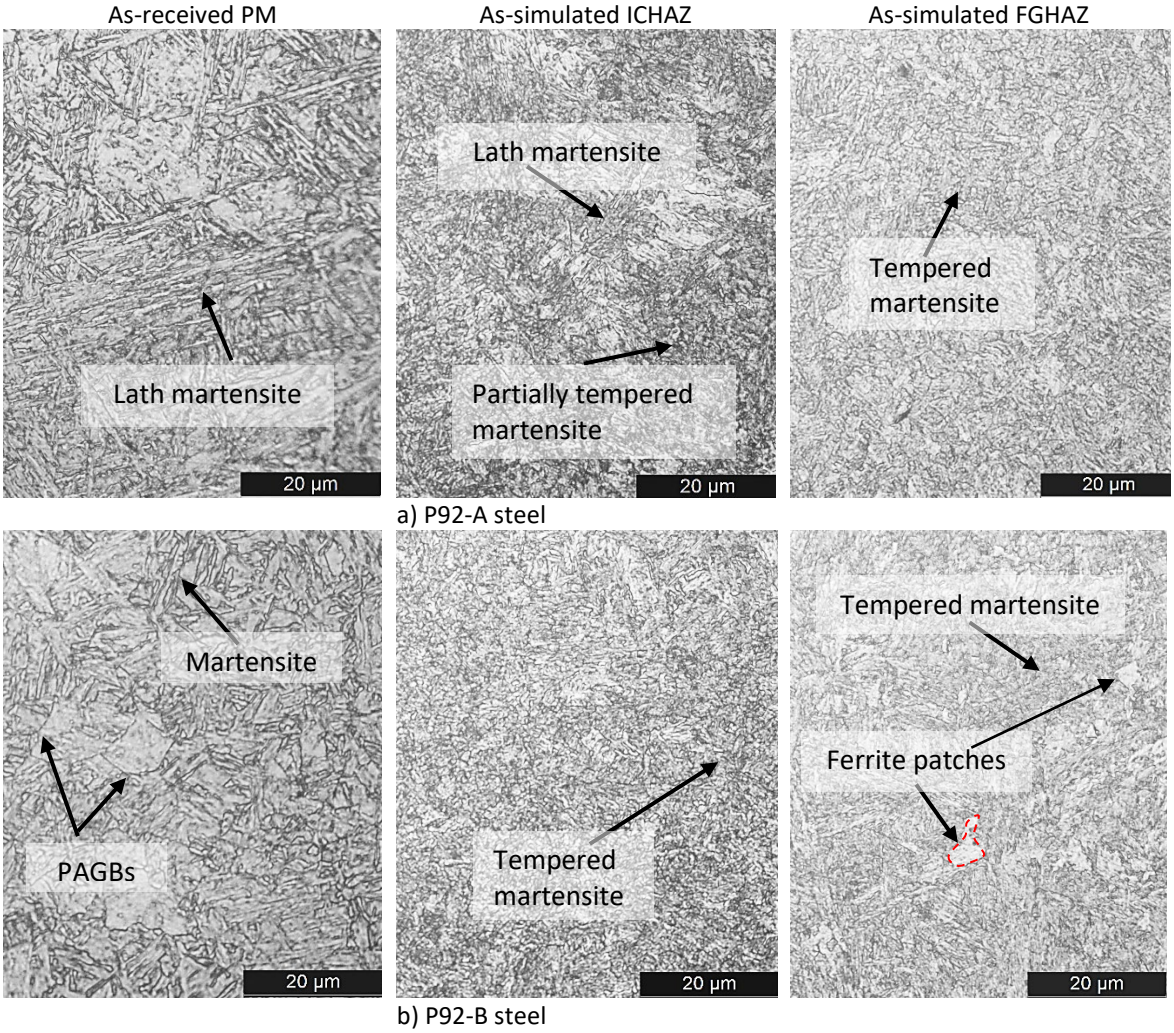

Fig. 8. Optical image of as-received parent metal and as-simulated HAZ microstructure.

Fig. 9 (ICHAZ) and **Fig. 10** (FGHAZ) show the SEM–BSE images of the simulated HAZ microstructures for the two steels. The as-simulated microstructure for the two steels shows untempered lath martensite with bright precipitates. The carbides observed suggest that the ICHAZ and FGHAZ peak temperatures caused the incomplete dissolution of carbides. There were undissolved bright coarse and fine carbides for the two HAZ regions (ICHAZ and FGHAZ) on the grain and lath boundaries. **Fig. 8** shows the ICHAZ microstructure of the two steels. Both steels exhibited untempered and partially tempered martensite. The simulated ICHAZ microstructures of the two steels were relatively similar: coarse precipitates (probably $M_{23}C_6$) on the lath boundaries, with new, small grains formed after ICHAZ simulation. Simulation at 900 °C took a very short time, and since this temperature was lower than the dissolution temperature of carbides, this may have resulted in no dissolution of precipitates, causing carbide coarsening. The lower peak temperature of ICHAZ may cause the formation of tempered and un-tempered martensite of the original parent metal (Pandey *et al.*, 2019).

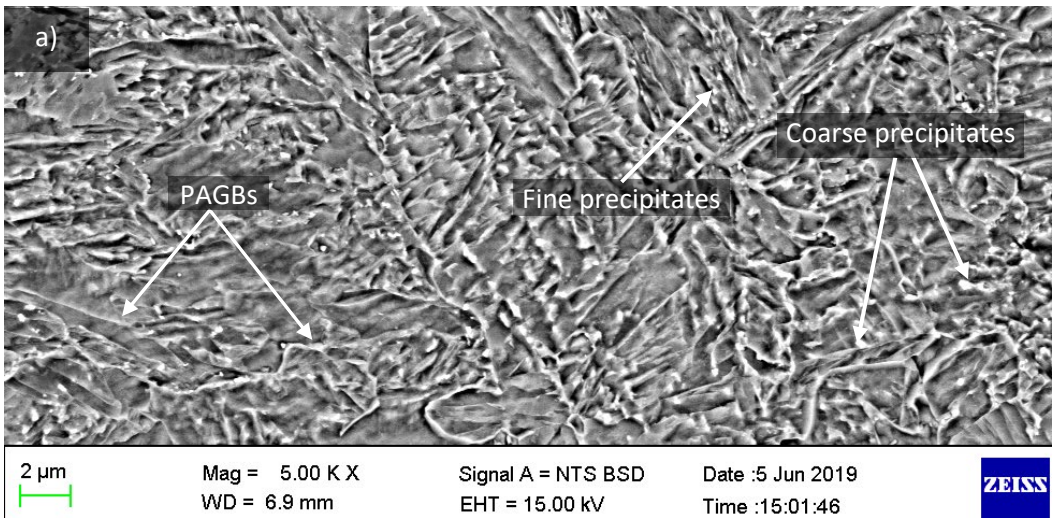

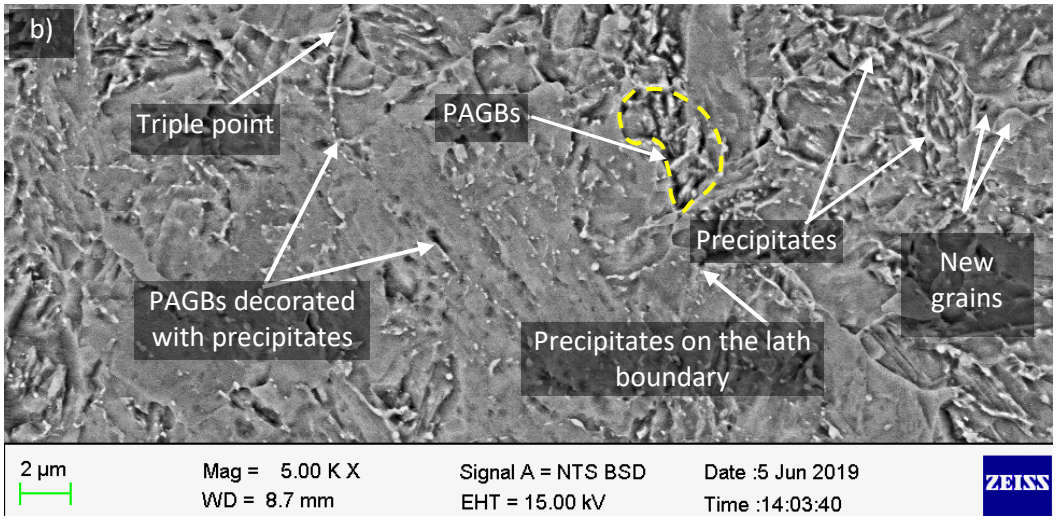

Fig. 9. SEM-BSE images of as-simulated ICHAZ a) P92-B and c) P92-C.

From **Fig. 10**, it is clear that FGHAZ and ICHAZ have similar microstructure for the two steels. The FGHAZ simulation samples experienced a peak temperature around the Ae_3 phase transformation temperature of P92 steel (~950 °C). At this peak temperature, partial dissolution of precipitates would occur, which enhanced the coarsening of undissolved carbides during the thermal cycle. Numerous carbides occurred along the lath boundaries. The dissolution temperature of the carbides in the two steels was below 930 °C, as determined from the empirical equation and reported by Peng *et al.*, (2017). However, the bright precipitates show that incomplete dissolution of carbides occurred, which was affected by the heating rate that increases the phase transformation temperature (Peng et al., 2017).

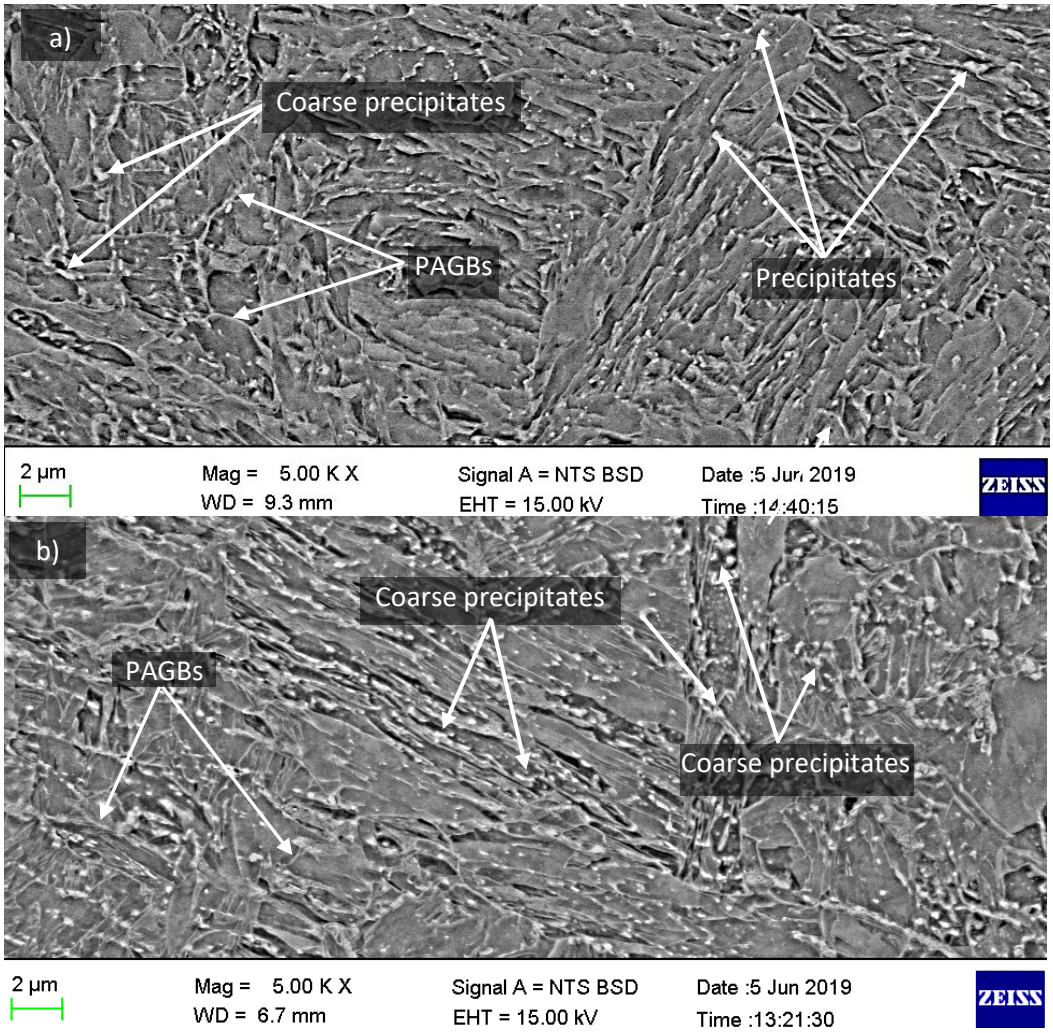

Fig. 10. SEM-BSE image of as-simulated FGHAZ a) P92-A steel b) P92-B steel.

The change in transformation temperature due to the heating rate was the reason for the incomplete dissolution of carbides that occurred after short-time peak temperature heating (950°C). FGHAZ microstructure exhibited clear grains and grain boundaries. The P92-B steel (**Fig. 10b**) had coarse precipitates in the as-simulated FGHAZ microstructure. The coarse particle perimeter measured by Image J software was 16.7 μm.

3.4 Microstructure of HAZ after PWHT

The micrographs of the parent metal and the simulated ICHAZ and FGHAZ, all after PWHT, are shown in **Fig. 11** for the two steels. After conventional PWHT, both steels exhibited tempered martensite microstructure for the parent metal and ICHAZ microstructures (**Fig. 11**). However, the martensite laths in the ICHAZ microstructure were slightly shorter than those in the as-received parent metal shown in **Fig. 11.** This result shows that grain refinement may have occurred due to heat treatment. The FGHAZ microstructure after PWHT had a finer and equiaxed grain, as shown in **Fig. 11**. This region is prone to Type IV cracking during long-term creep exposure. Hence, the characterisation and study of this region are paramount to mitigate weld joint failure for prolonged exposure. The parent metal exhibited tempered lath martensite after heat treatment, similar to the as-received condition (**Fig. 11**).

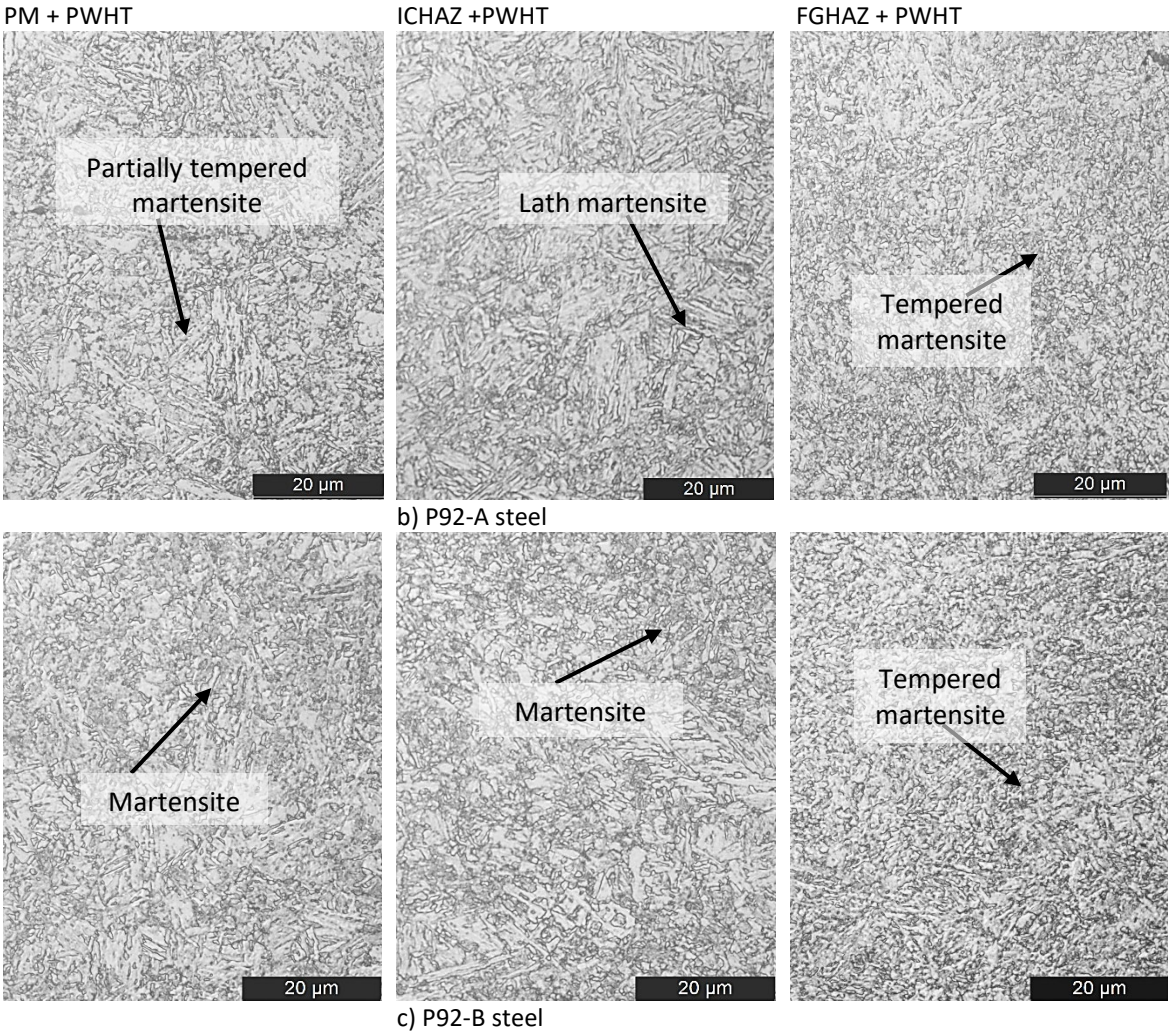

Fig. 11. Optical image of the as-received, ICHAZ and FGHAZ after PWHT for the two P92 steels.

Fig. 12 shows the SEM-BSE micrographs of the simulated ICHAZ after post-weld heat treatment. The steels had grain and lath boundaries having fine and coarse precipitates. The ICHAZ microstructure for the two steels exhibited fine and coarse carbides along the lath and prior austenite grain boundaries. During rapid heating and cooling in the HAZ simulation, some precipitates did not dissolve, and subsequent tempering caused the coarsening of the carbides, as shown in **Fig. 12**. The coarse carbides on the PAGBs caused the coarsening of the austenite grains as the boundaries became free from the pinning effect. Coarse precipitates show the location of the PAGBs of the parent metal. The carbides (normally $M_{23}C_6$ carbides) on the austenite grain boundaries provide the pinning effect during service conditions. The percentage area fraction of precipitates was 2.56 (P92-A) and 6.23(P92-B). The lower carbide percentage area fraction is due to the formation of large grain sizes. Large grain size formation reduces grain boundary formation, thus reducing the carbide precipitation process.

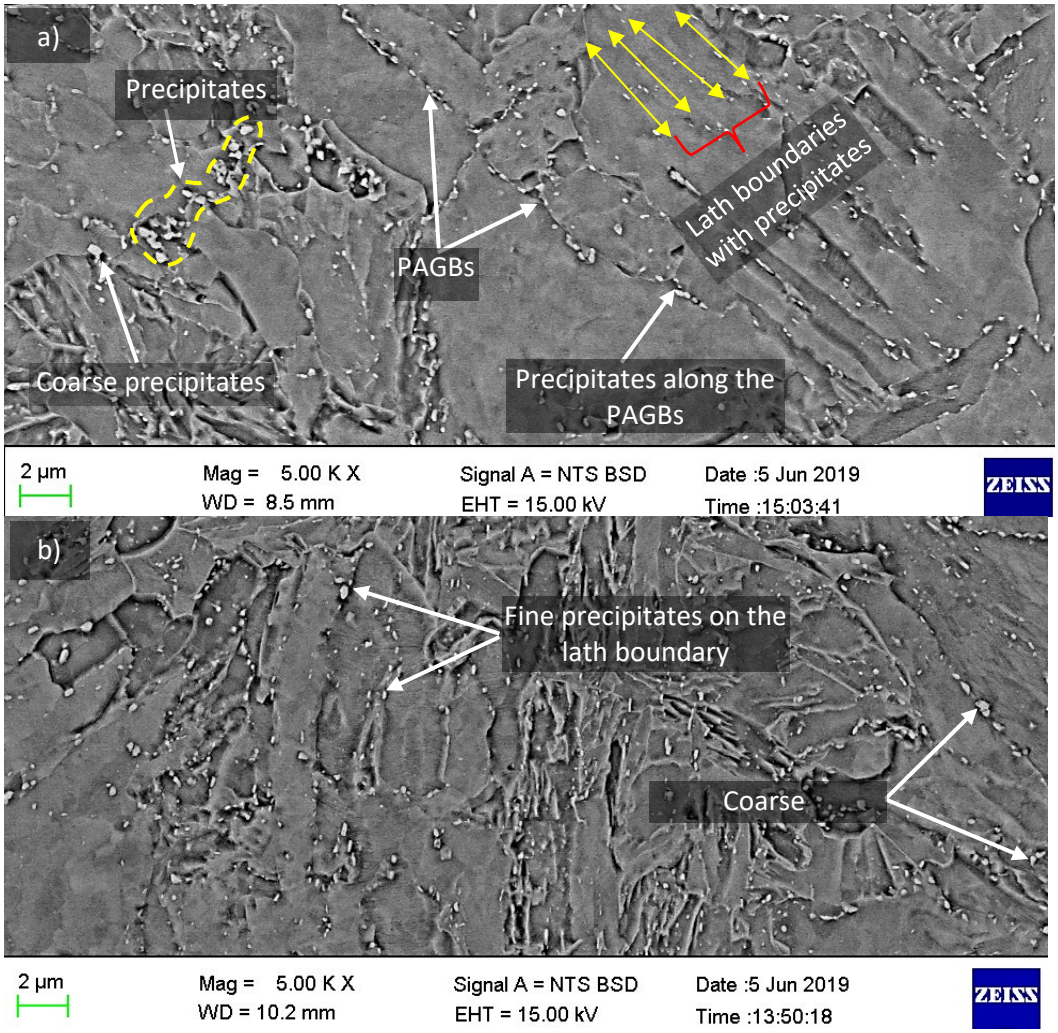

Fig. 12. SEM-BSE image of ICHAZ after PWHT a) P92-A b) P92-B.

The SEM-BSE micrographs of the simulated FGHAZ microstructure (T_p = 950°C) after PWHT are in **Fig. 13**. The two steels showed randomly distributed spheroidal fine and coarse precipitates. The formation of finer grains occurred due to the presence of undissolved carbides that pin the grain boundaries and prevent austenite grain growth (Pandey *et al.*, 2018). Prior austenite grain boundaries had sparsely distributed precipitates. **Fig. 13** for the two steels shows fewer precipitates on the grain boundaries, hence a lower pinning effect to dislocation movements, causing a reduction in material strength. Coarse carbides occurred along the grain boundaries for both ICHAZ and FGHAZ. These carbides act as the crack nucleation sites for Type IV cracking during creep (Parameswaran & Laha, 2013). The percentage area fraction of carbides was 0.44 (P92-A) and 1.08 (P92-B). The percentage area fraction of precipitates was 1.72 (P92-A) and 3.12 (P92-B).

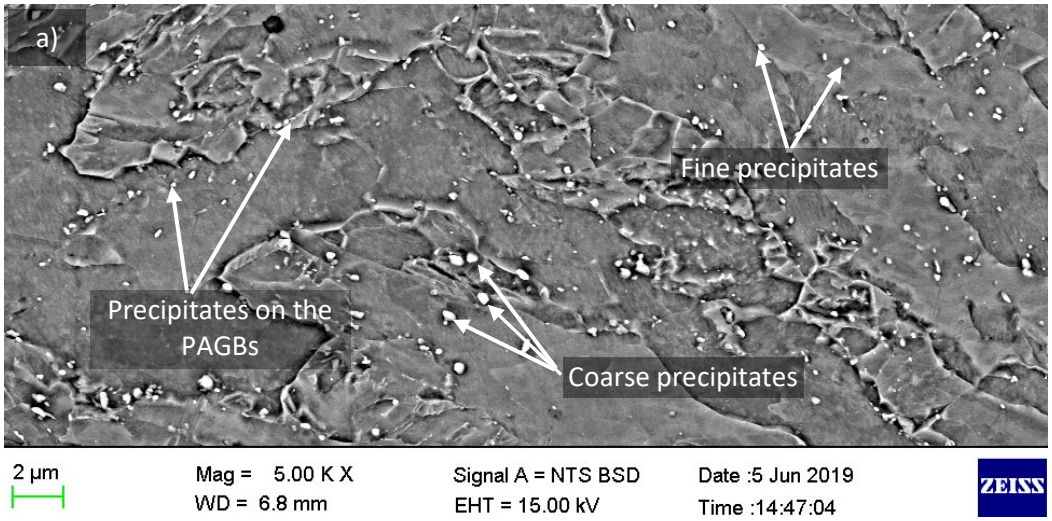

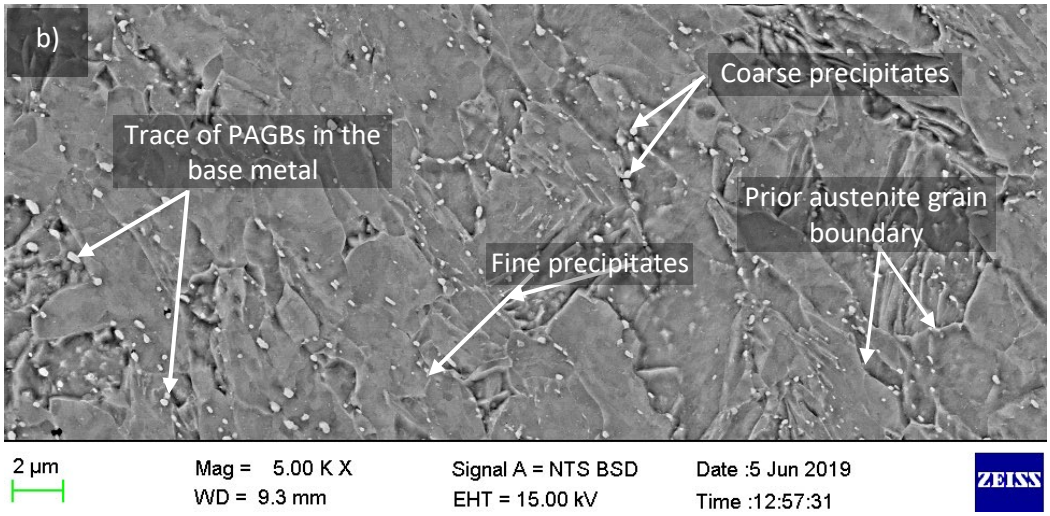

Fig. 13. SEM-BSE image of FGHAZ after PWHT a) P92-A steel and b) P92-B.

3.5 Microstructure of HAZ after r-PWHT

After r-PWHT, the heat-treated parent metal and the HAZ microstructures are in **Fig. 14**. The microstructures had tempered martensite and well-defined grain boundaries for both the parent metal and the HAZ regions. The parent metal and the simulated heat-affected zone samples exhibited identical microstructure.

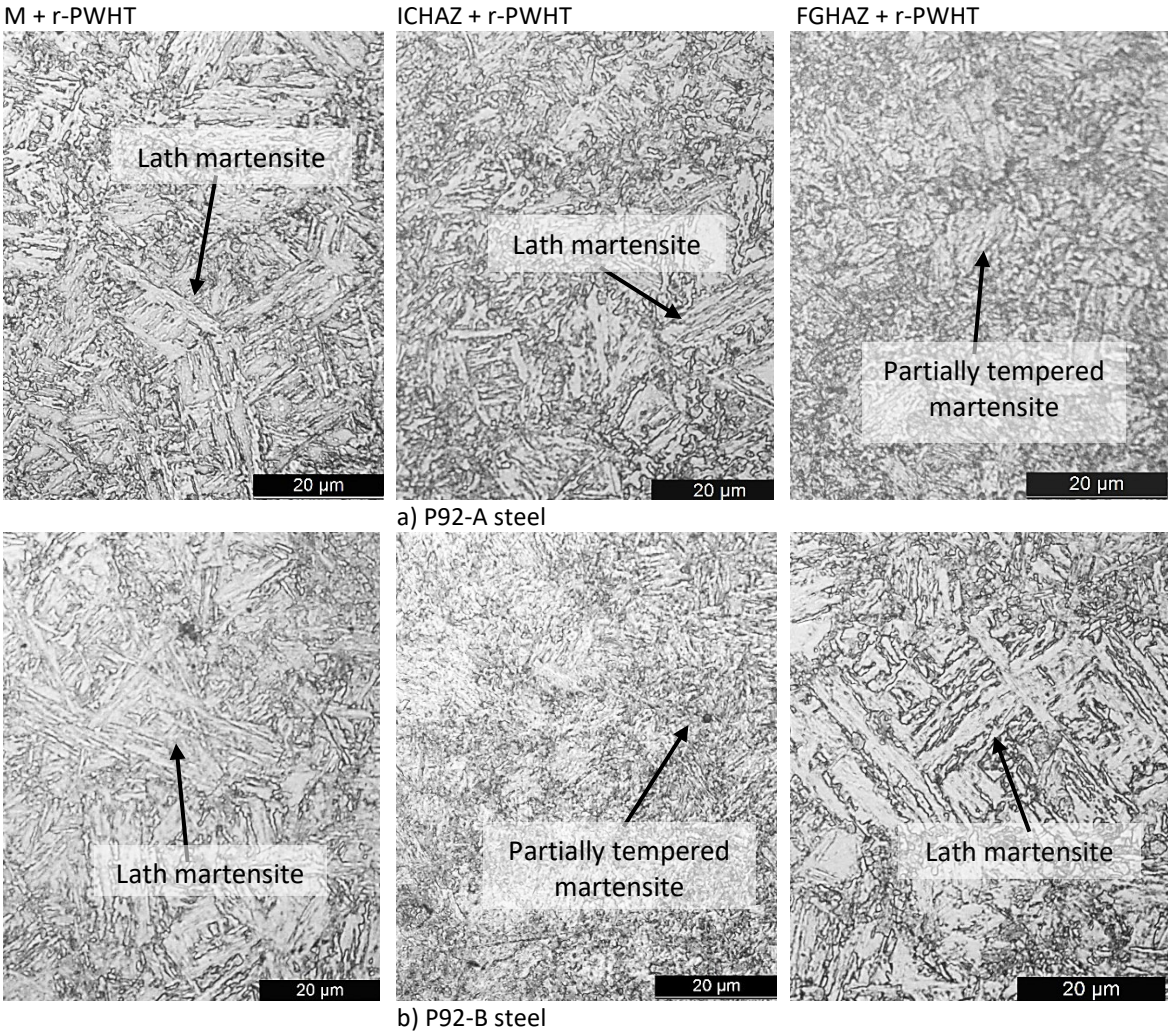

Fig. 14. Optical image of the as-received, ICHAZ, and FGHAZ after r-PWHT.

During welding simulation, complete carbide dissolution into the matrix occurs, leading to a homogeneous microstructure. The heating process occurring during welding is similar to austenitisation. After tempering, dislocation density and breaking

of laths occur, causing solid solution strengthening. Hence, a higher number of precipitates forms due to an increased number of grain boundaries. P92-A steel exhibited longer martensite laths for the parent metal and the ICHAZ than FGHAZ (**Fig. 14a**). This observation implies that ICHAZ had a microstructure similar to the parent metal. The FGHAZ microstructure had finer grains after r-PWHT. P92-B steel had a partially tempered martensitic structure (FGHAZ) like the parent metal (**Fig. 14 b**). The microstructure evolution in the HAZ region depends on the microalloying elements in the steel, hence affecting the phase transformation temperature. The results show that under the same heat treatment (r-PWHT), ICHAZ and the FGHAZ regions had different microstructures for the two steels. The study concluded that re-austenitisation after welding led to the microstructure homogenisation of the HAZ. However, this depends on the chemical composition, phase transformation temperature, and heating rate. The heating rate affects the phase transformation temperature, hence the dissolution of precipitates (Peng et al., 2017). Pandey *et al.* (2018) showed that normalisation after welding reverts the weld joint microstructure to be similar to that of the parent metal. Saini, Pandey and Mahapatra (2017) and Pandey *et al.* (2019) reported similar results. This heat treatment procedure is recommended in the production industry to prevent Type IV cracking. For example, Mitsubishi Heavy Industries (Japan) adapted this technology and reported that the cross-weld and parent metal had similar results after the creep test for 30,000 h and 700 °C for P91 steel (Abson & Rothwell, 2013).

The SEM-BSE micrographs for the ICHAZ and FGHAZ microstructures after r-PWHT are in **Figs. 15-16**. During re-austenitisation, the tempered martensite transforms into austenite on heating. On cooling, the austenite phase changes to untempered martensite. A complete dissolution of the carbides occurred during re-austenitisation. Dissolution of carbide makes the grain boundaries free from the pinning effect of carbides, thus allowing the growth of austenite grains. After tempering, precipitation of carbides occurs, improving precipitation strengthening. The re-austenitisation resulted in the homogenisation and a tempered martensite structure of the weld joint microstructure with carbides along the PAGBs and the lath boundaries, as shown in **Fig. 15-16.** The ICHAZ and FGHAZ microstructures of P92-A steel exhibited randomly distributed precipitates in the microstructure, as shown in Figures 15-16a). The P92-A had fewer coarse and fine precipitates **Figs. 15-16a**. The low number of carbides along the lath boundary and PAGBs indicates low precipitation of carbides. This observation implies that more carbon and nitrogen remained in the solid solution during tempering. Reduction in precipitates reduces the strengthening effect. The lower number of carbides after tempering may have been due to the effects of tempering temperature and time.

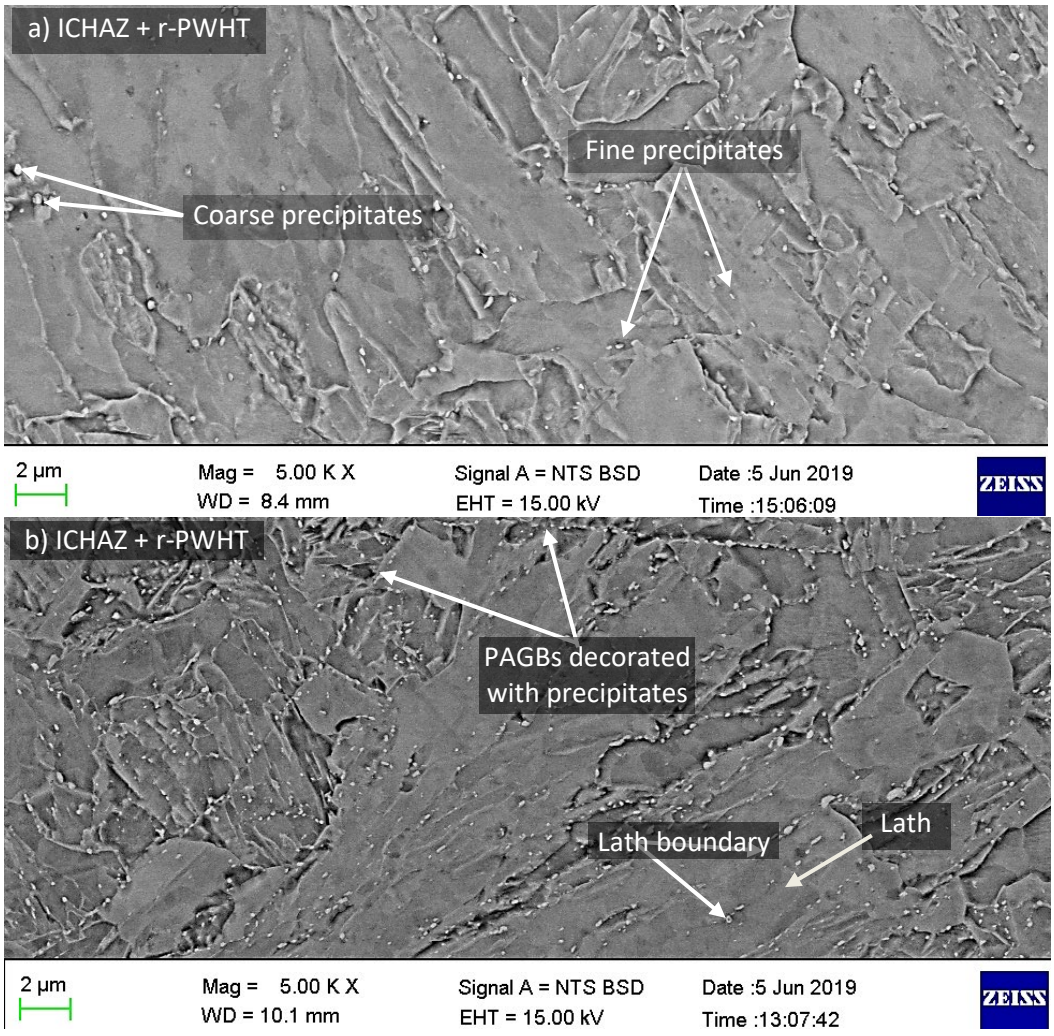

Fig. 15. SEM-BSE image of ICHAZ after r-PWHT a) P92-A b) P92-B.

Barbadikar *et al.* (2015) reported that an increase in the tempering temperature increases the area fraction of carbides, causing precipitation strengthening. An increase in the tempering time increases precipitates, as more carbon and nitrogen are removed from the solid solution to form carbides (Pandey & Mahapatra, 2016). Pandey, Giri and Mahapatra (2016) investigated the effect of varying tempering temperatures on phase evolution in P91 steel. The study noted that as the tempering time increased, more grains formed, causing an increase in carbides. They reported that an increase in the number of grain boundaries increases carbide precipitation. The tempering temperature and time in the current study were insufficient for complete carbide precipitation. The percentage area fraction of precipitates was 0.44 (P92-A) and 1.08 (P92-B) for ICHAZ, while 0.19 (P92-A) and 1.35 (P92-B) for FGHAZ. P92-B steel had tempered martensite after ICHAZ + r-PWHT (**Fig. 15b**). FGHAZ + r-PWHT (**Fig. 16b**) shows fine and coarse randomly distributed precipitates and lath martensite.

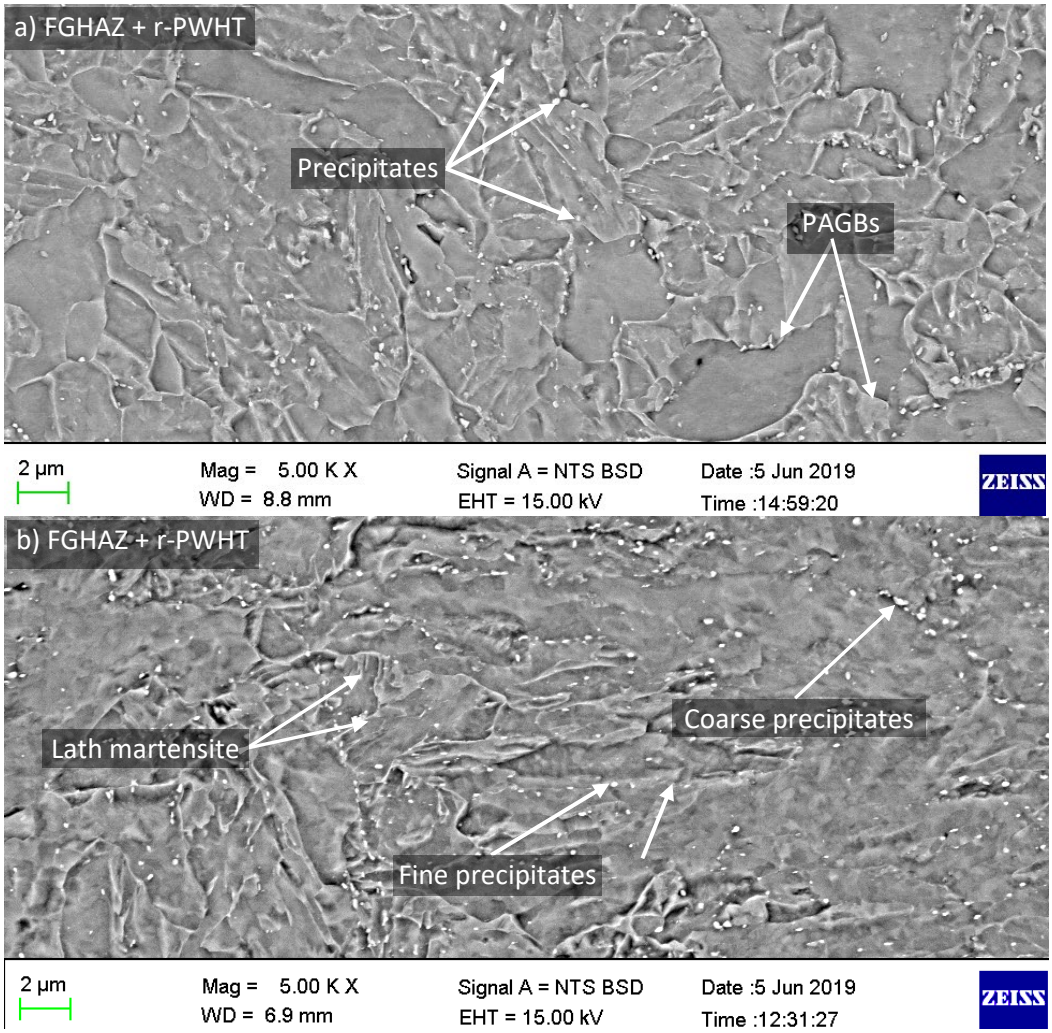

Fig. 16. SEM-BSE image of FGHAZ after r-PWHT a) P92-A b) P92-B.

3.6. Microhardness

The microhardness values of the two steels tested are shown in **Figs. 17-18**. The average hardness of the as-received steels was 234.8 ± 1.4 $HV_{0.5}$ (P92-A) and 231.4 ± 2.5 $HV_{0.5}$ (P92-B), as shown in Table 4. The HAZ simulation influences the microhardness values of as-simulated condition. **Fig. 17** shows that the hardness values for FGHAZ and ICHAZ. The results show that FGHAZ microstructure had higher microhardness values than the ICHAZ microstructure for the two steels. After heat treatment (PWHT), the hardness values were lower than in the as-welded condition, as shown in **Figs. 17-18.** Tempering decreased the hardness values (Saini et al., 2017). After tempering, hardness variation is a function of precipitate formation, grain size, and reduction in solid solution hardening (Pandey *et al.*, 2019). In actual welding, the FGHAZ hardness values of ~ 342-381 $HV_{0.5}$ were lower than the 404-480 $HV_{0.5}$ reported by Pandey *et al.* (2019). Thus, the peak temperature selected for the FGHAZ simulation was lower than the usual temperature in the FHGAZ region during actual welding. The hardness results showed a variation in hardness values after PWHT. These results indicate that after simulation, complete dissolution of carbides did not occur, and subsequent tempering caused carbide coarsening. This phenomenon reduces the precipitation, hence reducing the percentage area fraction of carbides. The ICHAZ had a lower hardness value (237.8 ± 4.1 $HV_{0.5}$) than FGHAZ (312.6 ± 40.7 $HV_{0.5}$) for P92-A steel after PWHT. The reason could be that ICHAZ had a higher percentage area fraction of precipitates (2.56) than FGHAZ (0.44). The variation in the area fraction of carbides indicates that FGHAZ had

higher solid solution hardening due to the low number of precipitates, hence high hardness. However, ICHAZ had a higher hardness value (283.2 ± 13.7 $HV_{0.5}$) than FGHAZ (271.9 ± 5.0 $HV_{0.5}$) for P92-B steel, even though ICHAZ had the highest area fraction of carbides (6.23). The area fraction of carbides is not the only factor contributing to high hardness values. Therefore, this implies that other factors may be contributing to hardness values. One reason could be carbide coarsening, which reduces the pinning effect on the austenite grain boundaries. The other reason can be the grain boundaries recovery, thus reduction of dislocation density (Wang et al., 2013).

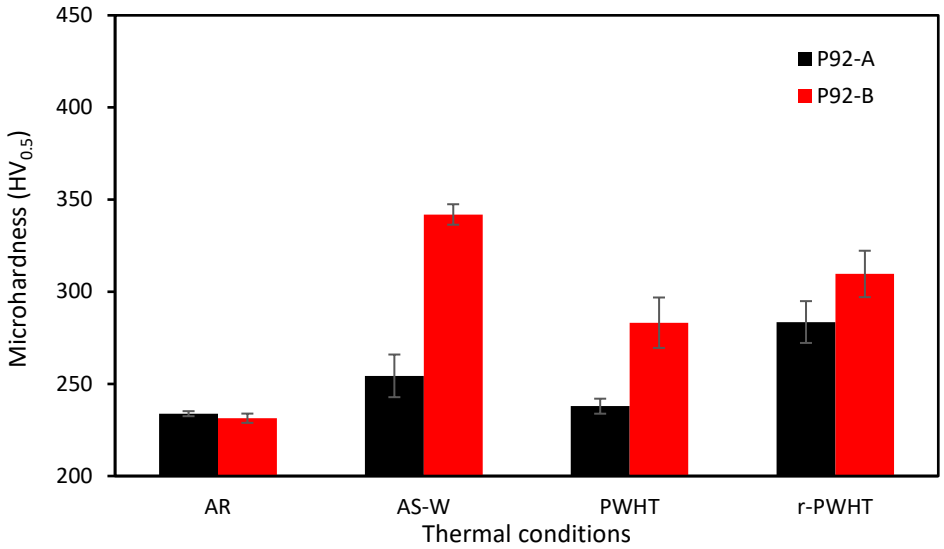

Fig. 17. Graph showing the microhardness values of ICHAZ at different test conditions.

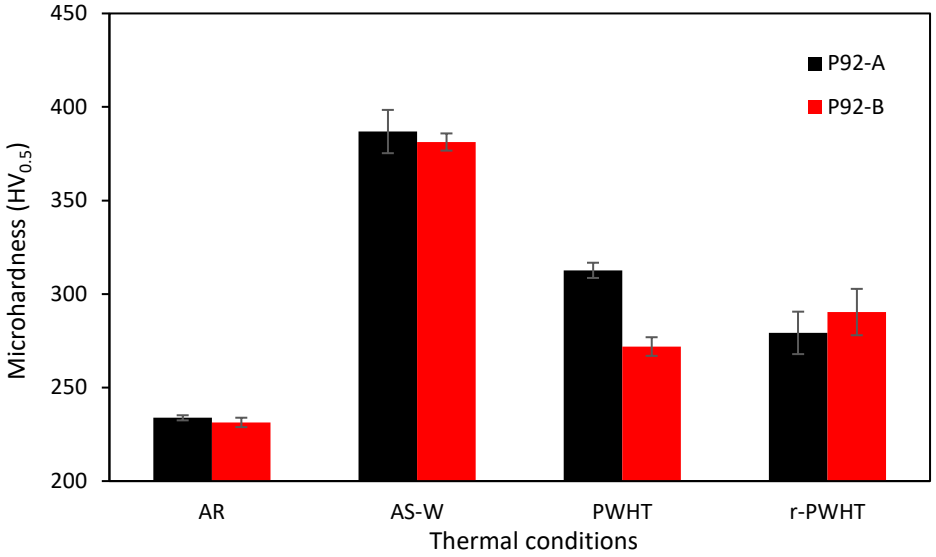

Fig. 18. Graph showing the microhardness values of FGHAZ at different test conditions.

After r-PWHT, the simulated HAZ microstructure further exhibited variation in the microhardness. **Table 4** shows the microhardness values for the two steels. After r-PWHT, FGHAZ microstructures for P92-A had the lowest microhardness value. The P92-B steel had the highest hardness values after heat treatments, as shown in **Table 4**. In general, heat treatment decreased the hardness of ICHAZ and FGHAZ in the two steels. The low hardness values were due to the softening of the formed brittle HAZ martensitic structure after the thermal cycle and the growth of the precipitates (Pandey *et al.* 2018).

Table 4. Summarised microhardness values of the two steels in different test conditions.

T_{max} (°C)	Condition	P92-A	P92-B
-	AR	233.8 ± 1.4	231.4 ± 2.5
ICHAZ	As-S	254.4 ± 11.6	341.9 ±5.6
	PWHT	237.8 ± 4.1	283.2 ± 13.7
	r-PWHT	283.6 ± 11.3	309.7 ± 12.6
FGHAZ	As-S	386.9 ± 17.5	381.3 ± 4.6
	PWHT	312.6 ± 40.7	271.9 ± 5.0
	r-PWHT	279.2 ± 18.7	290.4 ± 12.4

3.7 Charpy Impact Toughness

Table 5 shows the Charpy toughness values for ICHAZ and FGHAZ for all tested samples under different conditions. Figure 18 indicates the Charpy toughness values of the two steels investigated at different conditions. These results are for one sample per test. The test material was not enough to prepare more samples. However, the results were sufficient to provide the necessary required test data for analysing the material behaviour. The results show that in as-received (AR) condition, the sample had a Charpy toughness was 130J (P92-A) and 178J (P92-B), as shown in **Table 5**. As-simulated HAZ for both conditions had Charpy toughness value higher than 74J for the two steels. Therefore, the test samples had toughness value higher than the minimum toughness value of 47J required of the weld joint for the hydro-testing of vessels (Pandey *et al.* 2018). As-welded condition, the Charpy toughness values were relatively high (**Table 5**). The toughness values show that the microstructure did not transform into untempered brittle martensite during HAZ simulation. The SEM images show that the ICHAZ and FGHAZ microstructure after simulation a high precipitate amount, indicating the incomplete dissolution of carbides. This observation implies that the HAZ microstructure was over-tempered, causing a minor change in the microstructure. The microstructure changes resulted in martensite softening due to increased precipitation, hence a reduction in solid solution hardening (Pandey *et al.* 2019). For example, the Charpy toughness values for the two steels showed insignificant change after the HAZ simulation compared to the as-received metal. The P92-A had a higher toughness value than the as-received metal for ICHAZ. The results show that incomplete hardening did not occur. For the two HAZ conditions, peak temperatures only transformed the microstructure into over-tempered and partially tempered with a high density of undissolved precipitates.

Table 5. Charpy toughness values for the two steels under different test conditions.

T_{max} (°C)	Condition	P92-A	P92-B
-	AR	130	178
ICHAZ	As-S	158	138
	PWHT	145	83
	r-PWHT	154	74
FGHAZ	As-S	112	112
	PWHT	175	180
	r-PWHT	154	107

*The error bars are not given; one sample was tested due to insufficient material to prepare more samples and the table indicates Charpy toughness.

The ICHAZ for P92-A steel had higher toughness (158J) than the as-received metal (130J) and P92-B steel. The higher toughness values of ICHAZ for P92-A steel may be due to over-tempering of the martensite and precipitate coarsening. The simulated ICHAZ of P92-B steel had the lowest toughness values of 83J (PWHT) and 74J (r-PWHT). These lower toughness values showed that the formed martensite after heat treatment had new, brittle martensite from the fraction of transformed austenite. For the ICHAZ microstructure, incomplete dissolution of the $M_{23}C_6$ carbides occurred for P92-B steel. From Thermo-Calc analysis, the equilibrium dissolution temperature of $M_{23}C_6$ carbides is 911°C for P92-C steel. Heat treatment may have caused carbide coarsening, thus offering less resistance to impact loading. Higher hardness values were measured under the same test conditions, indicating a formation of brittle martensite. The microstructures of P92-B steel showed that precipitates were distributed unevenly, with few grain boundaries seen (**Fig. 12** and **Fig. 15**). The lower number of carbides shows the formation of brittle martensite after heat treatments, hence low resistance to impact loading. The FGHAZ showed an improved Charpy toughness after heat treatment (**Fig. 19b**). Improved toughness was due to softening of the martensite structure, together with an increased fraction of precipitates, hence a reduction in solid solution hardening.

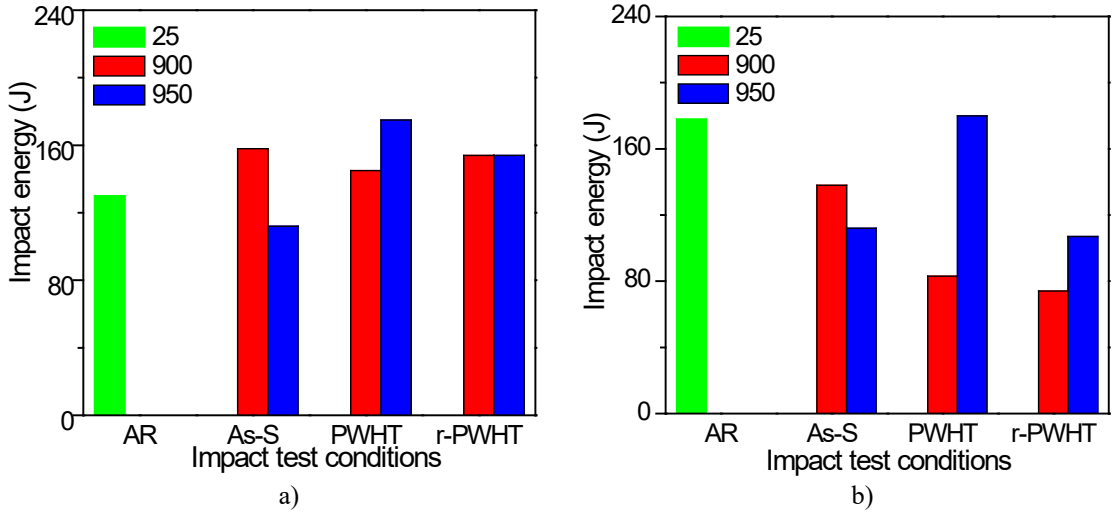

Fig. 19. Charpy toughness values at different processing conditions: a) P92-A and b) P92-B.

The Charpy toughness value for P92-A steel was 154J after r-PWHT treatment. This value was higher than that of the parent metal (130J), as shown in **Fig. 19a-b**). After austenitisation, the complete dissolution of carbides occurs. Tempering causes precipitation and softening of the formed brittle martensite structure. The microstructure under these conditions (FGHAZ/ICHAZ + r-PWHT) exhibited a tempered martensitic microstructure, as shown in **Figs. 15-16a**. The toughness values indicate that the simulated ICHAZ/FGHAZ microstructure homogenisation may have occurred after r-PWHT treatment (Pandey *et al.* 2019). P92-B steel had lower Charpy toughness values after r-PWHT than the base metal. The base metal had a fully tempered martensitic microstructure, hence a high Charpy toughness value. The poor toughness values may be due to δ-ferrite occurring along with tempered martensite (Moon et al., 2015).

3.7. Fracture surface morphology

3.7.1 P92-A steel

Fig. 20 shows the fracture surface of as-received P92-A steel after Charpy impact testing. The SEM-BSE image shows fracture surface characteristics such as microcracks, shear dimples, and tear ridges indicating ductile fracture. These features occur due to the coalescence of microvoids. The shear dimples indicate a tempered martensitic microstructure.
In the as-simulated ICHAZ sample, the ductile fracture mode was dominant, as confirmed by dimples, microvoids, and an area of shear (**Fig. 21a**). The results show that the ICHAZ sample had higher Charpy toughness (158J) than the parent metal (130J). The improved Charpy toughness (Figure 19b) occurs due to martensite over-tempering and carbide coarsening.

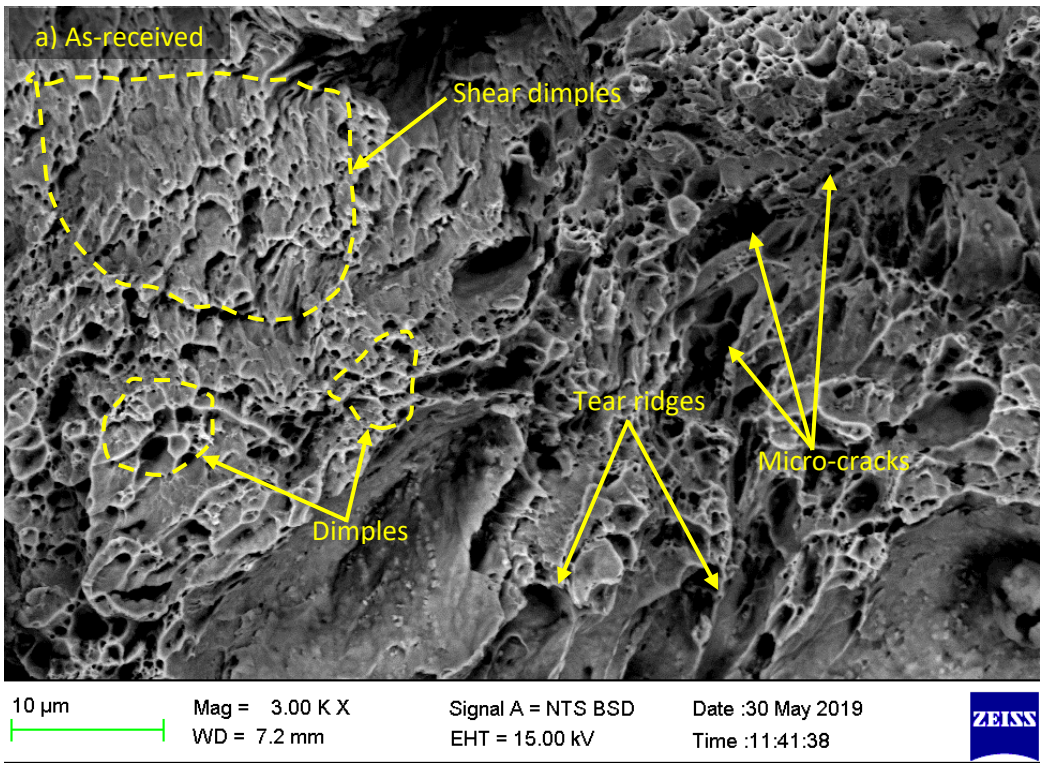

Fig. 20. SEM-BSE fractography image for P92-B steel.

The ICHAZ + PWHT (**Fig. 21b**) shows voids, quasi-cleavage facets, dimples, and micro cracks on the fracture surface, indicating a mixed fracture mode behaviour. After ICHAZ + PWHT, the microstructure had tempered martensite with precipitates along the grain boundaries, which resulted in a lower hardness value (237.9 ± 4.1 HV05) and higher Charpy toughness value (145J). ICHAZ + r-PWHT (Figure 21c), ductile fracture occurred, as shown on the fracture surface. Under this heat treatment condition (ICHAZ + r-PWHT), the fracture changed from mixed fracture mode observed in ICHAZ + PWHT condition to ductile mode. These toughness values indicate that r-PWHT may have increased the precipitation due to an increase in grain boundaries (**Fig. 15a**), hence increasing toughness from 145J (PWHT) to 154J (r-PWHT).

Fig. 22a shows the fracture surface image of the as-simulated FGHAZ microstructure. The micrograph shows microcracks, quasi-cleavage facets, and tear ridges. These microstructural features indicate untempered lath martensite (X. Wang et al., 2016). The low HAZ simulation peak temperature may have caused solid solution hardening, hence the lower toughness value. The failure behaviour was a characteristic of brittle fracture mode caused by enhanced solid-solution hardening due to limited precipitation.

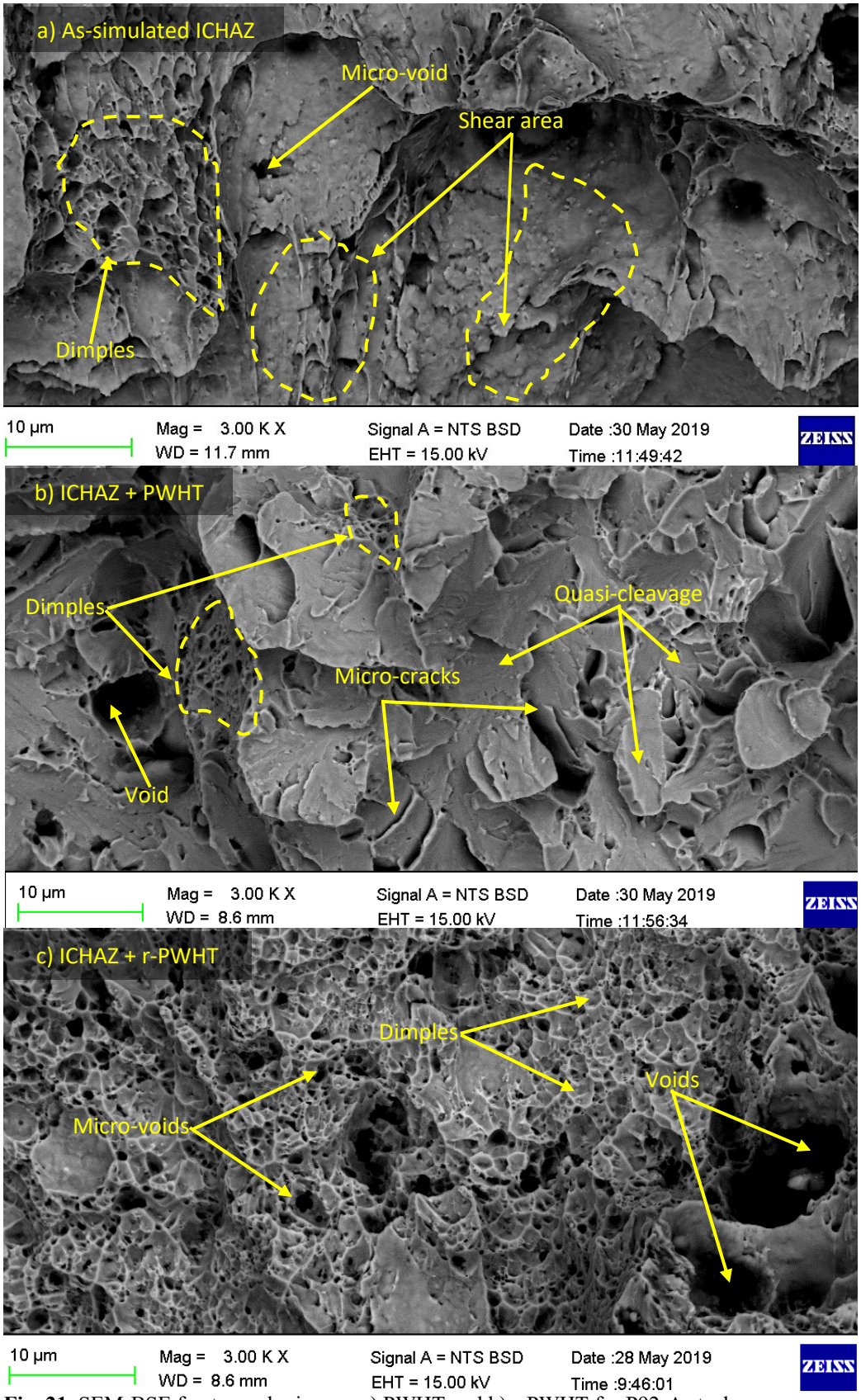

Fig. 21. SEM-BSE fractography image: a) PWHT and b) r-PWHT for P92-A steel.

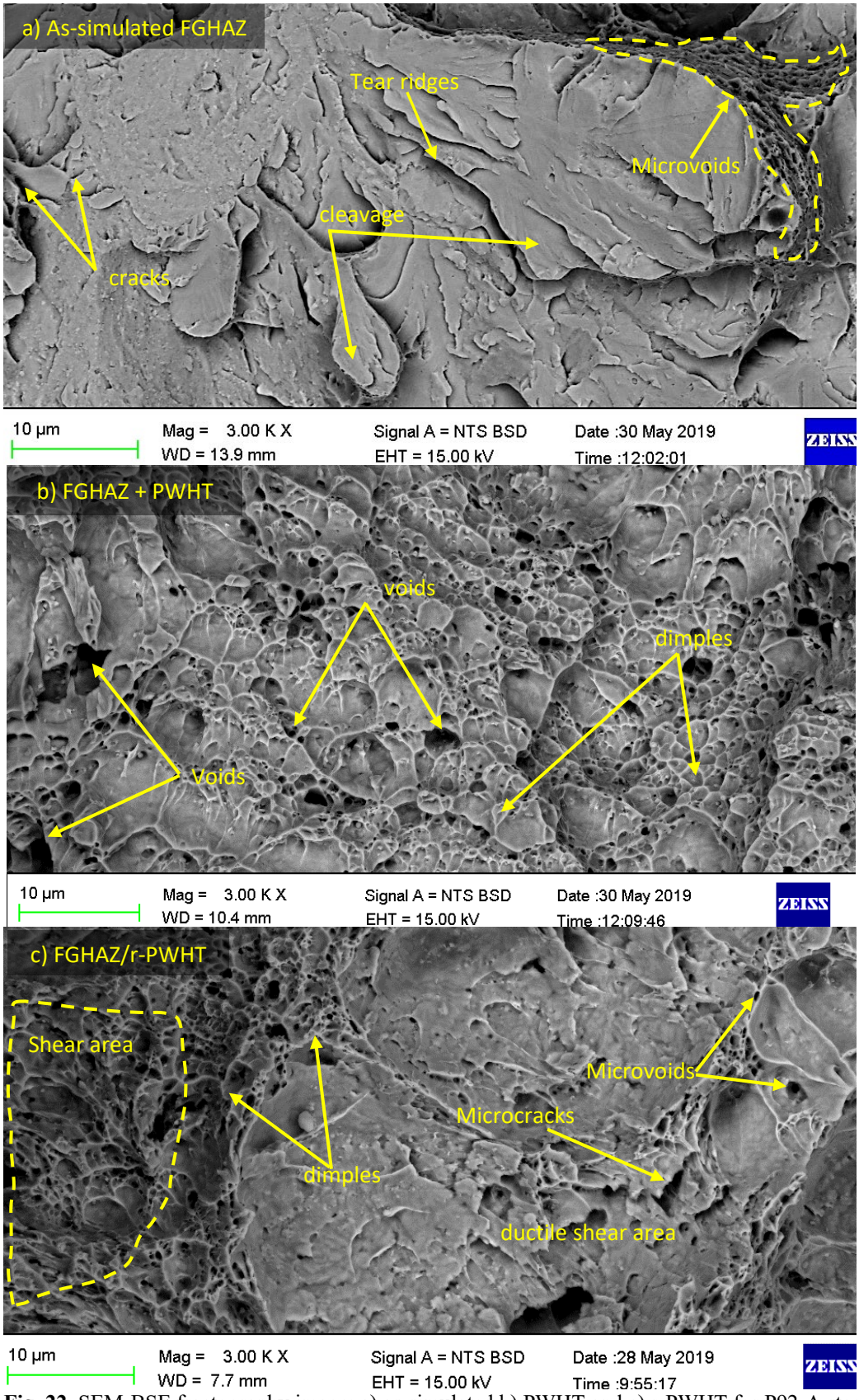

Fig. 22. SEM-BSE fractography image: a) as-simulated b) PWHT and c) r-PWHT for P92-A steel.

However, the FGHAZ + PWHT and FGHAZ + r-PWHT conditions showed ductile fracture mode with dimples, microvoids, voids, and shear (**Fig. 22 b-c**). The FGHAZ sample in these two conditions had improved fracture behaviour. After r-PWHT, all HAZ samples had the same fracture toughness value (154J), and hardness values were relatively close, with a difference of 4.7 ± 7.4 $HV_{0.5}$. These hardness results show that homogeneous microstructure occurred after r-PWHT,

having uniform austenite grain sizes and alloying element redistribution caused by suppression of both structural and chemical gradient (Falat et al., 2016).

3.7.2 P92-B steel

Fig. 23 shows the fracture surface of the Charpy toughness sample tested at room temperature for as-received P92-B steel**.** The BSE-SEM micrograph shows the presence of microcracks, shear area, and reduced dimple sizes, indicating ductile fracture mode. As simulated ICHAZ, the fracture surface (Figure 24a) had microvoids and ductile dimples showing a ductile fracture mode. However, the fracture mechanism of the as-simulated ICHAZ after PWHT and r-PWHT changed from ductile to brittle fracture mode, as shown in Figure 24(b-c). Under these heat treatment conditions (PWHT and r-PWHT), the fracture surface appeared to have more area occupied by quasi-cleavage and tear ridges than ductile dimples (Figure 24b-c). The brittle fracture behaviour after tempering shows that carbon and nitrogen were not ejected from the matrix, causing solid solution hardening. The trapped C and N in the matrix resulted in untempered martensite. The untempered martensite was due to insufficient time to achieve a complete tempering. Pandey and Mahapatra (2016) reported that tempering time enhances the mechanical properties of a material due to solid solution strengthening. However, they noted that increasing tempering time beyond 8 hours at a tempering temperature of 760 °C caused a reduction of precipitates. As mentioned earlier, precipitate reduction affects the mechanical behaviour of the material, especially creep resistance, toughness, and hardness. In this study, P92-B steel had high hardness and low Charpy toughness values for the tested conditions. These mechanical responses may be due to reduced solid solution strengthening.

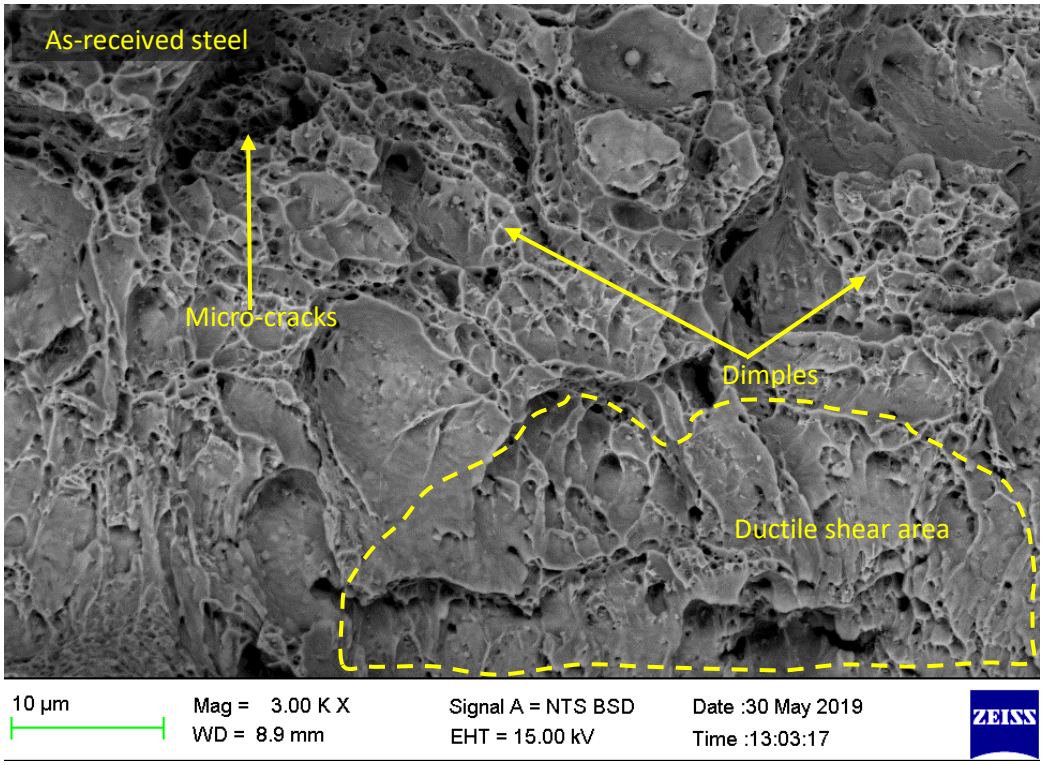

Fig. 23. SEM-BSE fractography image as-received P92-B steel.

The fractography image of the as-simulated FGHAZ exhibited cleavage and a small area fraction of dimples, indicating a brittle fracture mode, as shown in **Fig. 25a**. The FGHAZ + PWHT fracture surface had quasi-cleavage, tear ridges, micro-cracks, and microvoids, indicating brittle fracture, as shown in Figure 25b. FGHAZ + r-PWHT (**Fig. 25c**) shows that the fracture mode changed to ductile. The micro-cracks, microvoids, and ductile dimple tearing observed result from microvoids coalescence, as shown in **Fig. 25c**. Generally, the ICHAZ-treated samples had the lowest Charpy toughness values. The variation in fracture toughness may be due to the fracture events ahead of the crack tip, such as voids, cracks, and inclusions. Microcracks, microvoids, and decohesion of the particle/matrix interface within the crack processing zone may have affected the fracture mode during testing.

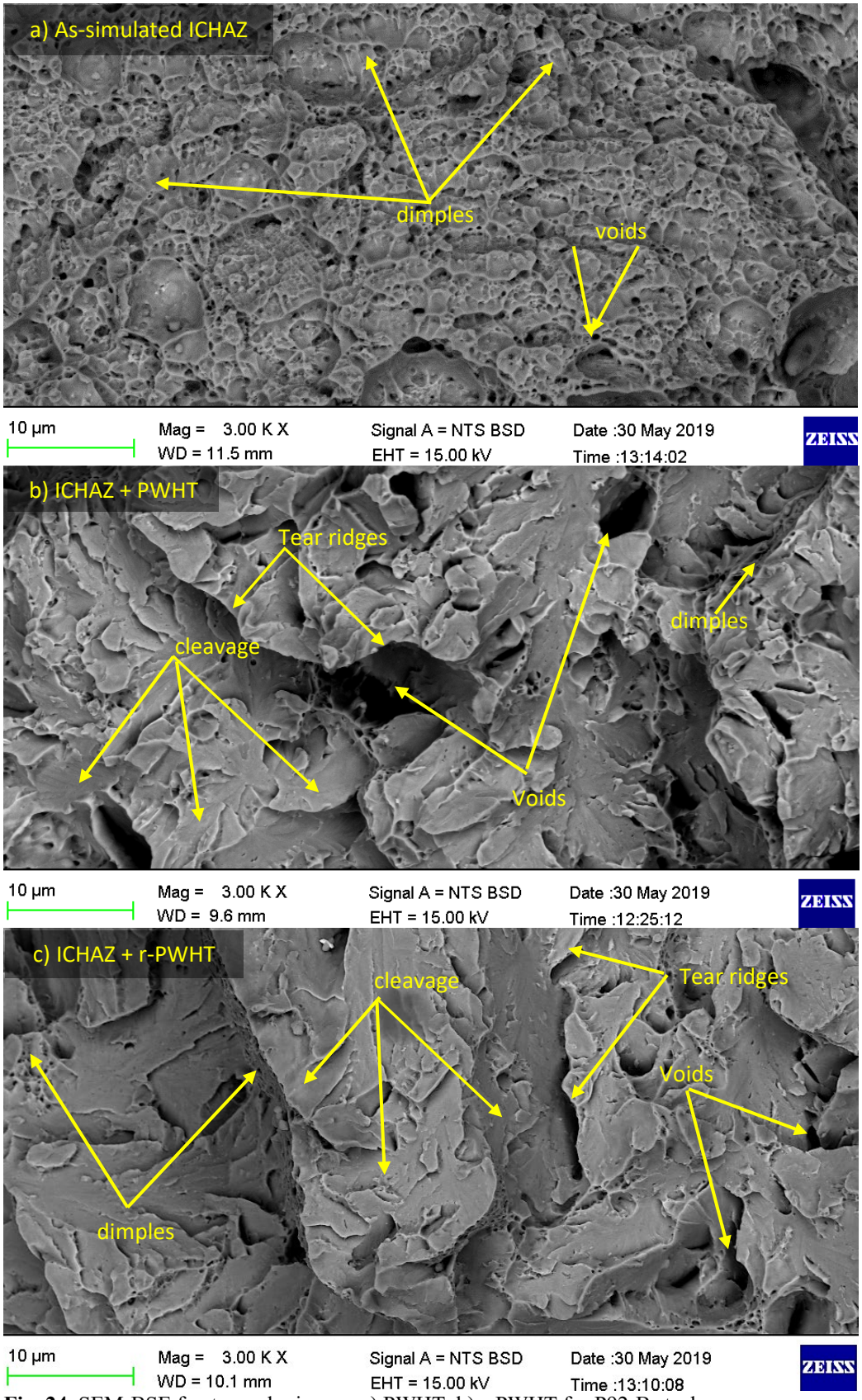

Fig. 24. SEM-BSE fractography image: a) PWHT, b) r-PWHT for P92-B steel.

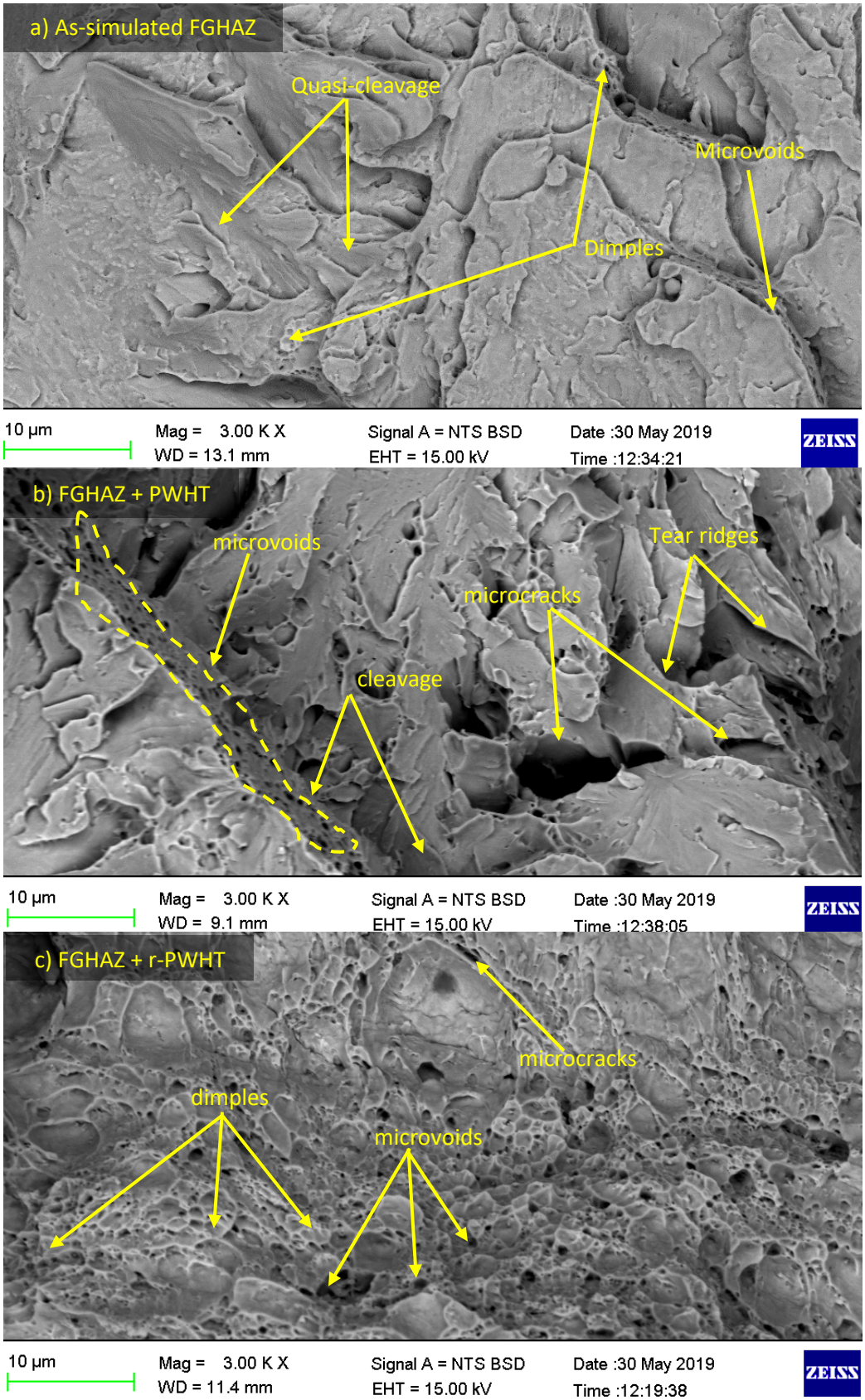

Fig. 25. SEM-BSE fractography image a) as-simulated, b) PWHT, and c) r-PWHT for P92-B steel.

5. Conclusion

This study investigated the influence of heat treatment schedule, especially a combination of Normalisation and Tempering (N + T) of two P92 steel with chromium and tungsten content variations. From the study, the authors made the following observation:

1. The Thermo-Calc analysis showed that the carbide dissolution temperature is 888 °C (P92-A) and 911°C (P92-B). At ICHAZ and FGHAZ peak temperatures, $M_{23}C_6$ carbides will dissolve, and subsequent heat treatment causes precipitation and coarsening of carbides. However, the heating rate raised the dissolution temperature, causing carbide coarsening during the physical simulation for the two steels.
2. As-simulated ICHAZ and FGHAZ for the two steels had untempered martensite and undissolved carbides, which started growing. After heat treatment, the weld joints (HAZ) exhibited tempered martensitic microstructure. The lath and grain boundaries had fine and coarse carbides.
3. As-received samples of the two steels had hardness values of 234.8 ± 1.4 $HV_{0.5}$ (P92-A) and 231.4 ± 2.5 $HV_{0.5}$ (P92-B). In the as-simulated condition, the hardness values for the two steels were 254 ± 7 $HV_{0.5}$ (P92-A) and 341.9 ±5.6 $HV_{0.5}$ P92-B for ICHAZ and 386.9 ± 17.5 $HV_{0.5}$ (P92-A) and 381.3 ± 4.6 $HV_{0.5}$ (P92-B) for FGHAZ. After the FGHAZ simulation, the hardness of the two steels were quite similar. Generally, P92-B had the highest hardness values after heat treatment except at FGHAZ + PWHT condition, which had a lower hardness value (271.9 ± 5.0 $HV_{0.5}$). This condition (FGHAZ + PWHT) for P92-B also had the highest Charpy impact toughness value (180J), higher than as received base metal. This result indicates that P92-B steel had a fully martensite microstructure.
4. As-received samples of P92-A had Charpy toughness of 130J, while P92-B had 178J. As simulated conditions (ICHAZ and FGHAZ), the two steels had Charpy toughness ranging between 112-158J. ICHAZ for P92-A steel had higher toughness (158J) than the as-received metal (130J). After heat treatment, ICHAZ + PWHT, the Charpy toughness values were 145J (P92-A) and 83J (P92-B). The improved toughness for P92-A was due to tempered martensite microstructure formation and a high area fraction of precipitates. The microstructure exhibited solid solution strengthening. FGHAZ + PWHT, the Charpy toughness were 175J (P92-A) and 180J (P92-B). These values were higher than those of the parent metals. The higher toughness value may be due to over-tempering of the martensite and precipitate coarsening in two steels.
5. After ICHAZ + r-PWHT, P92-A had a higher toughness value 154J compared to 74J for P92-B. P92-B had the lowest toughness values in all heat treatment conditions (PWHT and r-PWHT). The lower toughness values were due to new and brittle martensite, which formed due to higher carbon content in the matrix. FGHAZ + r-PWHT, P92-A steel had higher toughness values of 154J than the parent metal (130J). P92-B steel had a toughness value of 107J, lower than the parent metal (178J). However, in all the test conditions, the Charpy toughness results were higher than the recommended 47J of the weld joint required for hydro-testing of the vessels.
6. Generally, no marked results were observed in the two steel regardless of the variation in chromium and tungsten content. This heat treatment method is applicable in the industry for Type IV crack mitigation of the weld joint.

Acknowledgement

The authors appreciate DSI-CSIR Interbursary Support (IBS) for financial support.

References

Abson, D. J., & Rothwell, J. S. (2013). Review of type IV cracking of weldments in 9–12%Cr creep strength enhanced ferritic steels. *International Materials Reviews*, *58*(8), 437–473. https://doi.org/10.1179/1743280412Y.0000000016

Albert, S. K., Matsui, M., Watanabe, T., Hongo, H., Kubo, K., & Tabuchi, M. (2003). Variation in the type IV cracking behaviour of a high Cr steel weld with post weld heat treatment. *International Journal of Pressure Vessels and Piping*, *80*(6), 405–413. https://doi.org/10.1016/S0308-0161(03)00072-3

ASTM E 23-12c. (2012). Standard test methods for notched bar impact testing of metallic materials. In *Standards: Vol. i*. https://doi.org/10.1520/E0023-12C.2

Barbadikar, D. R., Deshmukh, G. S., Maddi, L., Laha, K., Parameswaran, P., Ballal, A. R., Peshwe, D. R., Paretkar, R. K., Nandagopal, M., & Mathew, M. D. (2015). Effect of normalizing and tempering temperatures on microstructure and mechanical properties of P92 steel. *International Journal of Pressure Vessels and Piping*, *132–133*, 97–105. https://doi.org/10.1016/j.ijpvp.2015.07.001

Barbadikar, D. R., Sakthivel, T., Ballal, A. R., Peshwe, D. R., Syamala Rao, P., & Mathew, M. D. (2018). An assessment of mechanical properties of P92 steel weld joint and simulated heat affected zones by ball indentation technique. *Materials at High Temperatures*, *35*(5), 427–437. https://doi.org/10.1080/09603409.2017.1371913

Chalk, K. M., Shipway, P. H., & Allen, D. J. (2011). Austenite formation during heat treatment of P92 power plant steel welds: Dependence of A1 temperature on compositional changes. *Science and Technology of Welding and Joining*, *16*(7), 613–618. https://doi.org/10.1179/1362171811Y.0000000042

Czyrska-filemonowicz, A., Zielińska-lipiec, A., & Ennis, P. J. (2006). Modified 9 % Cr Steels for Advanced Power Generation : Microstructure and Properties. *Journal of Achievements in Materials and Manufacturing Engineering*, *19*(2), 43–48.

Dunđer, M., Vuherer, T., Samardžić, I., & Marić, D. (2019). Analysis of heat-affected zone microstructures of steel P92 after welding and after post-weld heat treatment. *International Journal of Advanced Manufacturing Technology*, *102*(9–12), 3801–3812. https://doi.org/10.1007/s00170-019-03513-8

Ennis, P. J., & Czyrska-Filemonowicz, A. (2003). Recent advances in creep-resistant steels for power plant applications. *Sadhana - Academy Proceedings in Engineering Sciences*, *28*(3–4), 709–730. https://doi.org/10.1007/BF02706455

Esposito, L. (2016). Type IV creep cracking of welded joints: numerical study of the grain size effect in HAZ. *Procedia Structural Integrity*, *2*, 919–926. https://doi.org/10.1016/j.prostr.2016.06.118

Falat, L., Kepič, J., Čiripová, L., Ševc, P., & Dlouhý, I. (2016). The effects of postweld heat treatment and isothermal aging on T92 steel heat-affected zone mechanical properties of T92/TP316H dissimilar weldments. *Journal of Materials Research*, *31*(10), 1532–1543. https://doi.org/10.1557/jmr.2016.134

Francis, J. A., Mazur, W., & Bhadeshia, H. K. D. H. (2006). Type IV cracking in ferritic power plant steels. In *Materials Science and Technology* (Vol. 22, Issue 12, pp. 1387–1395). https://doi.org/10.1179/174328406X148778

Gleeble. (1999). Gleeble Manual QuickSimTM HAZ Programming Manual and Samples, DSI Dynamic System Inc. In *Gleeble and Hydrawedge Quicksim, Poestenikll, NewYork, USA,* (pp. 1–26).

Guo, Q., Lu, F., Liu, X., Yang, R., Cui, H., & Gao, Y. (2015). Correlation of microstructure and fracture toughness of advanced 9Cr/CrMoV dissimilarly welded joint. *Materials Science and Engineering: A*, *638*, 240–250. https://doi.org/10.1016/j.msea.2015.04.011

Gutiérrez, N. Z., Alvarado, J. V., de Cicco, H., & Danón, A. (2015). Microstructural Study of Welded Joints in a High Temperature Martensitic-ferritic ASTM A335 P91 Steel. *Procedia Materials Science*, *8*(1992), 1140–1149. https://doi.org/10.1016/j.mspro.2015.04.178

Hasegawa, Y., Sugiyama, M., & Kawakami, K. (2009). Type Iv Damage Mechanism Due To The Microstructure Weakening In The Haz Of A Multi-Layer Welded Joint Of The W Containing 9 % Cr Ferritic Creep Resistant Steel. *Ommi*, *6*(2), 1–16.

Hurtado-noreña, C., Danón, C. A., Luppo, M. I., & Bruzzoni, P. (2015). Evolution of Minor Phases in a P91 Steel Normalized and Tempered at Different Temperatures. *Procedia Materials Science*, *8*, 1089–1098. https://doi.org/10.1016/j.mspro.2015.04.172

Kim, H., Inoue, J., Okada, M., & Nagata, K. (2017). Prediction of Ac3 and martensite start temperatures by a data-driven model selection approach. *ISIJ International*, *57*(12), 2229–2236. https://doi.org/10.2355/isijinternational.ISIJINT-2017-212

Lim, B. S., Jeong, C. S., & Keum, Y. T. (2003). Effect of Temperature on Fatigue Crack Growth in P92 Steel. *Metals and Materials International*, *9*(6), 543–547. https://doi.org/10.1007/BF03027253

Liu, Y., Tsukamoto, S., Sawada, K., & Abe, F. (2014). Role of boundary strengthening on prevention of type IV failure in high Cr ferritic heat-resistant steels. *Metallurgical and Materials Transactions A: Physical Metallurgy and Materials Science*, *45*(3), 1306–1314. https://doi.org/10.1007/s11661-013-2072-5

Liu, Y., Tsukamoto, S., Shirane, T., & Abe, F. (2013). Formation mechanism of type IV failure in high Cr ferritic heat-resistant steel-welded joint. *Metallurgical and Materials Transactions A: Physical Metallurgy and Materials Science*, *44*(10). https://doi.org/10.1007/s11661-013-1801-0

Łomozik, M., & Zielińska-Lipiec, A. (2008). Microscopic Analysis of the Influence of Multiple Thermal Cycle on Simulated HAZ Toughness in P91 Steel. *Archives of Metallurgy and Materials*, *53*(4), 1025–1034.

Milović, L., Vuherer, T., Blačić, I., Vrhovac, M., & Stanković, M. (2013). Microstructures and mechanical properties of creep resistant steel for application at elevated temperatures. *Materials and Design*, *46*, 660–667. https://doi.org/10.1016/j.matdes.2012.10.057

Moon, J., Lee, C. H., Lee, T. H., & Kim, H. C. (2015). Effect of Heat Input on Microstructure Evolution and Mechanical Properties in the Weld Heat-Affected Zone of 9Cr-2W-VTa Reduced Activation Ferritic-Martensitic Steel for Fusion Reactor. *Metallurgical and Materials Transactions A: Physical Metallurgy and Materials Science*, *46*(1), 156–163. https://doi.org/10.1007/s11661-014-2623-4

Nagode, A., Kosec, L., Ule, B., & Kosec, G. (2011). Review of creep resistant alloys for power plant applications. In *Metalurgija* (Vol. 50, Issue 1, pp. 45–48).

Ohgami, M., Naoi, H., Kinbara, S., Mimura, H., Ikemoto, T., & Fujita, T. (1997). Development of 9CrW tube, pipe and forging for ultra supercritical power plant boilers. In *Nippon Steel Technical Report* (Issue 72, pp. 59–64).

Pandey, C., Giri, A., & Mahapatra, M. M. (2016). Effect of normalizing temperature on microstructural stability and mechanical properties of creep strength enhanced ferritic P91 steel. *Materials Science & Engineering A*, *657*, 173–184. https://doi.org/10.1016/j.msea.2016.01.066

Pandey, C., & Mahapatra, M. M. (2016). *Evolution of phases during tempering of P91 steel at 760ºC for varying tempering time and their effect on microstructure and mechanical properties*. *0*(0), 1–21. https://doi.org/10.1177/0954408916656678

Pandey, C., Mahapatra, M. M., Kumar, P., Daniel, F., & Adhithan, B. (2019). Softening mechanism of P91 steel weldments using heat treatments. *Archives of Civil and Mechanical Engineering*, *19*(2), 297–310. https://doi.org/10.1016/j.acme.2018.10.005

Pandey, C., Mahapatra, M. M., Kumar, P., & Saini, N. (2018a). Homogenization of P91 weldments using varying normalizing and tempering treatment. *Materials Science and Engineering A*, *710*(June 2017), 86–101. https://doi.org/10.1016/j.msea.2017.10.086

Pandey, C., Mahapatra, M. M., Kumar, P., & Saini, N. (2018b). Some studies on P91 steel and their weldments. In *Journal of Alloys and Compounds* (Vol. 743, pp. 332–364). Elsevier B.V. https://doi.org/10.1016/j.jallcom.2018.01.120

Pandey, C., Mohan Mahapatra, M., Kumar, P., Thakre, J. G., & Saini, N. (2019). Role of evolving microstructure on the mechanical behaviour of P92 steel welded joint in as-welded and post weld heat treated state. *Journal of Materials Processing Technology*, *263*(June 2018), 241–255. https://doi.org/10.1016/j.jmatprotec.2018.08.032

Parameswaran, P., & Laha, K. (2013). Role of microstructure on creep rupture behaviour of similar and dissimilar joints of

modified 9Cr-1Mo steel. *Procedia Engineering*, *55*, 438–442. https://doi.org/10.1016/j.proeng.2013.03.277

Peng, Y. Q., Chen, T. C., Chung, T. J., Jeng, S. L., Huang, R. T., & Tsay, L. W. (2017). Creep rupture of the simulated HAZ of T92 steel compared to that of a T91 steel. *Materials*, *10*(2). https://doi.org/10.3390/ma10020139

Ryu, S. H., & Yu, J. (1998). A new equation for the Cr equivalent in 9 to 12 pct Cr steels. *Metallurgical and Materials Transactions A: Physical Metallurgy and Materials Science*, *29*(6), 1573–1578. https://doi.org/10.1007/s11661-998-0080-7

Saini, N., Pandey, C., & Mahapatra, M. M. (2017). Characterization and evaluation of mechanical properties of CSEF P92 steel for varying normalizing temperature. *Materials Science and Engineering A*, *688*(February), 250–261. https://doi.org/10.1016/j.msea.2017.02.022

Sakthivel, T., Laha, K., Chandravathi, K. S., Parameswaran, P., Tailor, H. M., Vasudevan, M., & Mathew, M. D. (2014). Integrity assessment of grade 92 welded joint under creep condition. *Procedia Engineering*, *86*, 215–222. https://doi.org/10.1016/j.proeng.2014.11.031

Shankar, V., Mariappan, K., Sandhya, R., & Mathew, M. D. (2013). Evaluation of low cycle fatigue damage in grade 91 steel weld joints for high temperature applications. *Procedia Engineering*, *55*, 128–135. https://doi.org/10.1016/j.proeng.2013.03.231

Sklenička, V., Kuchařová, K., Svobodová, M., Kvapilová, M., Král, P., & Horváth, L. (2016). Creep properties in similar weld joint of a thick-walled P92 steel pipe. *Materials Characterization*, *119*, 1–12. https://doi.org/10.1016/j.matchar.2016.06.033

Tabuchi, M., Watanabe, T., Kubo, K., Matsui, M., Kinugawa, J., & Abe, F. (2001). Creep crack growth behavior in the HAZ of weldments of W containing high Cr steel. *International Journal of Pressure Vessels and Piping*, *78*(11–12), 779–784. https://doi.org/10.1016/S0308-0161(01)00090-4

Tanaka, Y., Kubushiro, K., Takahashi, S., Saito, N., & Nakagawa, H. (2013). Creep-induced microstructural changes in large welded joints of high Cr heat resistant steel. *Procedia Engineering*, *55*, 41–44. https://doi.org/10.1016/j.proeng.2013.03.216

Trzaska, J. (2015). Empirical formulae for the calculation of austenite supercooled transformation temperatures. *Archives of Metallurgy and Materials*, *60*(1), 182–185. https://doi.org/10.1515/amm-2015-0029

Vodopivec, F., Jenko, M., Celin, R., & Skobir, D. A. (2011). *Creep Resistance of Microstructure of Welds of Creep Resistant Steels*. *45*(2), 6–10.

Wang, S. S., Peng, D. L., Chang, L., & Hui, X. D. (2013). Enhanced mechanical properties induced by refined heat treatment for 9Cr-0.5Mo-1.8W martensitic heat resistant steel. *Materials and Design*, *50*, 174–180. https://doi.org/10.1016/j.matdes.2013.01.072

Wang, X., Li, Y., Li, H., Yang, C., & Yang, Q. X. (2016). Mechanical properties of T23 steel welded joints without post-weld heat treatment for fossil fired boilers. *Journal of Materials Research*, *31*(24), 4000–4008. https://doi.org/10.1557/jmr.2016.423

Wang, X., Xu, Q., Liu, H. wei, Liu, H., Shang, W., Ren, Y. yao, & Yu, S. min. (2014). The method for reproducing fine grained HAZ of W strengthened high Cr steel. *Materials Science and Engineering A*, *589*, 50–56. https://doi.org/10.1016/j.msea.2013.09.064

Xue, W., Pan, Q. gang, Ren, Y. yao, Shang, W., Zeng, H. qiang, & Liu, H. (2012). Microstructure and type IV cracking behavior of HAZ in P92 steel weldment. *Materials Science and Engineering A*, *552*, 493–501. https://doi.org/10.1016/j.msea.2012.05.076

Xue, W., Qian-Gang, P., Zhi-Jun, L., Hui-Qiang, Z., & Yong-Shun, T. (2011). Creep rupture behaviour of P92 steel weldment. *Engineering Failure Analysis*, *18*(1), 186–191. https://doi.org/10.1016/j.engfailanal.2010.08.020

Zhao, L., Jing, H., Xiu, J., Han, Y., & Xu, L. (2014). Experimental investigation of specimen size effect on creep crack growth behavior in P92 steel welded joint. *Materials and Design*, *57*, 736–743. https://doi.org/10.1016/j.matdes.2013.12.062